UCLouvain

epl

École polytechnique de Louvain

Thermal management of blue GaN-based nanoporous VCSELs

Author: **Clémentine Gevers**
Supervisors: **Laurent Francis, Jung Han**
Reader: **Denis Flandre**
Academic year 2021–2022
Master [120] in Electrical Engineering

Abstract

In this work a model on Comsol Multiphysics®, from Comsol Inc. has been presented to model the heat transport in nanoporous blue GaN-based VCSELs. Today, more than 100 million VCSELs are produced annually. However blue GaN VCSELs are still challenging because of the bottom mirror that shows high thermal conductivity or low electrical conductivity or demanding epitaxial processes.

Nanoporous distributed Bragg mirrors are analysed and modeled to improve the thermal resistance of the mirror. This kind of mirror is very promising since it is electrically conductivity and the fabrication of this DBR is not as challenging as other mirrors (epitaxial or dielectric).

Lowering the temperature in the VCSEL is the key element to reach continuous wave operation since the heating in the device is the main limitation. By lowering the temperature in the device, the performance of the VCSELs are expected to be increased.

The main temperature-dependent parameters that are analysed are the thermal wavelength shift and the decrease of the differential quantum efficiency.

Acknowledgements

Throughout my travel to become an engineer, I had the chance to meet outstanding people who have helped me grow and arrive at the conclusion of my master thesis. During my stay in New Haven, I had the privilege to work in close contact with a group of very talented people that made my international experience constructive either from a human and academic point of view.

First of all I would like to express my deepest gratitude to Professor Han who has accepted me as a master student in his group at Yale University and for all his encouragement.

I would like to extend my sincere appreciation to Prof. Laurent Francis for his guidance and supervision during the past few months. I am also grateful to Prof. Denis Flandre for his availability to be a part of my jury and to read my final work.

My sincere thanks to Rami Elafandy for his advise, availability, and consistent guidance. I will always be grateful for his teachings, patience, and support. I cannot leave Yale university without mentioning Jin-Ho, Bingjun, Chenziyi, Hao and Krishnaa for sharing their office, knowledge, and kindness.

I gratefully acknowledge the support of the International Lhoist Berghmans Innovation Chair that made all this exchange possible.

List of acronyms

VCSELs vertical cavity surface emitting lasers

CW continous-wave

UCSB University of California Santa Barbara

NP nanoporous

QW quantum well

QB quantum barrier

LED light emitting diode

EELs edge-emitting lasers

MQWs multiple quantum wells

DBRs distributed Bragg reflectors

ITO indium thin oxide

SRH Shockley-Read-Hall

NCTU National Chiao Tung University

ECE electrochemical etching

PECE photoelectrochemical etching

Contents

1 Introduction **1**

2 Blue GaN VCSELs and porous DBR: state of the art **3**

2.1 Blue GaN VCSEL . . . 4
2.1.1 III-nitride materials . . . 4
2.1.2 Fundamentals of vertical-cavity surface-emitting lasers . . . 6
2.1.3 GaN based VCSELs and DBR . . . 13
2.2 Nanoporous DBR and VCSELs: fundamentals and advantages . . . 17
2.2.1 Formation of porous GaN . . . 17
2.2.2 Fabrication of nanoporous (NP) DBR VCSELs . . . 20
2.2.3 Brief summary of NP DBR VCSELs . . . 21
2.3 Achieving Continuous-Wave (CW) Operation for NP GaN VCSELs 22
2.3.1 The heat equation . . . 22
2.3.2 Effects of heating . . . 23
2.3.3 Thermal management . . . 25

3 Simulations: Thermal modeling of VCSELs in COMSOL **29**

3.1 COMSOL thermal application . . . 31
3.2 Literature example . . . 32
3.3 Hypothesis . . . 33
3.3.1 Thermal conductivity and refractive index . . . 33
3.3.2 Effective DBR layer . . . 33
3.3.3 Steady-state simulation . . . 34
3.3.4 Heat exchange and sources . . . 35
3.4 Device configuration and dimensions . . . 36
3.5 Material properties . . . 39
3.6 Boundary conditions . . . 40
3.6.1 Thermal boundaries . . . 40
3.6.2 Axial symmetry . . . 40
3.7 Meshing principles . . . 41
3.8 Simulation results and flux analysis . . . 42

3.9 Validation with already working VCSELs . . . 47

4 Simulations and optimization **49**
4.1 Influence of parameters . . . 50
4.1.1 From pulsed to CW . . . 51
4.1.2 Bottom DBR width . . . 53
4.1.3 Number of pairs of the bottom DBR . . . 55
4.1.4 Porosity . . . 56
4.1.5 Aperture . . . 59
4.1.6 Cavity length . . . 63
4.1.7 Substrate thickness . . . 65
4.1.8 Mechanical stress analysis . . . 67
4.2 Perspectives . . . 69
4.2.1 Optimization of the thermal management . . . 69
4.2.2 Flip-chip . . . 73

5 Influence of the temperature on optical performances **75**
5.1 Wavelength shift analysis . . . 76
5.1.1 Transfer Matrix Method (TMM) . . . 76
5.1.2 Matlab program . . . 77
5.1.3 Results . . . 79
5.2 Impact on optical transduction . . . 80

6 Discussion **82**

7 Conclusion **84**

Chapter 1

Introduction

The concept of vertical cavity surface emitting lasers (VCSELs) was first proposed in 1977 by Professor Kenichi Iga from Tokyo Institute of Technology. Two years later he achieved lasing for the first time under pulsed condition at 77K.[1] Today, more that 100 million VCSELs are produced annually and the price for such a laser for computer-mouse applications is approaching $0.10. [2, 3]

VCSELs have become popular light sources due to their many advantages: low power consumption, single longitudinal emission, on-wafer testing ... The well-established GaAs and InP VCSELs emits in the infrared regime. GaN-based VCSEL can however emit over the whole spectrum due to the unique properties of III-nitride materials.

The interest for short wavelengths (400-500 nm) VCSELs in many fields has been growing: data communication systems[4, 5], miniature atomic clocks [1] and medical applications. Low power blue lasers are used, in dentistry to detect carries.[6] In the field of medical diagnosis, the detection of skin and esophagus cancer is now possible without the use of biopsy by using laser-induced fluorescence at a wavelength of 410 nm [7]. This is why the fabrication of blue VCSELs is a very promising field. Many ways to fabricate these blue VCSELs have been proposed. In this thesis the nanoporous VCSELs will be analysed in detail.

Master thesis objectives

An important problem with nanoporous GaN (NP-GaN) VCSELs is their inability to lase under continous-wave (CW) operation; meaning that it fails if it is turned on longer than a few milliseconds. This is a severe limitation for most application of VCSELs. Its inability to lase under CW operation is due to the increase of

the temperature in the device.[8] The goal of this research is thus to improve the thermal management of the NP GaN-based VCSEL.

This thesis is thus focussing on the thermal management of VCSELs. It has already been done by other research groups: [8, 9, 10] However the thermal analysis of NP GaN-based VCSELs has never been explored before.

The objective of this thesis will thus be to reduce the temperature and thermal resistance of the device by optimizing the structure, based on finite element method (FEM) simulations using a commercially available tool Comsol Multiphysics®, from Comsol Inc. Furthermore, an investigation on the optical properties of the NP GaN VCSEL is proposed. The main figures of merit that will be analysed are the wavelength emission and wavelength shift with temperature as well as the optical transduction.

Master thesis outline

This master thesis is organized as follows:

- **Chapter 2** reviews the state of the art of porous GaN VCSELs. It first starts with the fundamentals of III-nitride materials and blue GaN-based VCSELs, focussing on the challenges of the DBR mirror. Next the fabrication and advantages of nanorporous GaN and distributed Bragg reflectors (DBR) are discussed. It finishes with the effect of heating and a review of the proposed solutions in the literature to reach CW operation.
- **Chapter 3** explains the steps to create the thermal model in COMSOL. It also validates the model by comparing the results to values found in the literature.
- **Chapter 4** studies the impact of multiple parameters on the maximum temperature and thermal resistance of the device. It concludes with perspectives to improve the thermal management, based on the results of the simulations.
- **Chapter 5** analyses the impact of the temperature on the optical performances. First with a transfer matrix method (TMM) that computes the thermal wavelength shift. Next the impact on the optical transduction is evaluated.
- **Chapter 6** discusses the results of previous chapters and summarizes the scientific findings.
- **Chapter 7** concludes this thesis with some future perspectives.

Chapter 2

Blue GaN VCSELs and porous DBR: state of the art

Contents

2.1 Blue GaN VCSEL **4**
2.1.1 III-nitride materials 4
2.1.2 Fundamentals of vertical-cavity surface-emitting lasers . 6
2.1.3 GaN based VCSELs and DBR 13
2.2 Nanoporous DBR and VCSELs: fundamentals and advantages **17**
2.2.1 Formation of porous GaN 17
2.2.2 Fabrication of NP DBR VCSELs 20
2.2.3 Brief summary of NP DBR VCSELs 21
2.3 Achieving Continuous-Wave (CW) Operation for NP GaN VCSELs **22**
2.3.1 The heat equation 22
2.3.2 Effects of heating 23
2.3.3 Thermal management 25

Overview

This chapter reviews the literature about NP GaN-based VCSELs. It first starts with a section that serves as a theoretical walk-through for concepts related to this project. Next the fabrication of porous GaN and NP GaN-based VCSELs is explained. It finishes with a review of the achievement to reach CW operation.

2.1 Blue GaN VCSEL

The first section starts with an introduction to the III-nitride materials and their properties. Next a brief introduction to the working principle of lasers is given and applied to vertical cavity surface emitting lasers (VCSELs). The third section explains the basic concepts of GaN VCSELs and the challenges related to the DBR.

2.1.1 III-nitride materials

III-nitride materials are semiconductor materials such as InN,GaN, AlN and their alloys. To reach the octet rule, metals with three valence electrons (Al, In, Ga, B) are combined with nitrogen, which has 5 valence electrons. Together they have proved to be great materials for photoelectric devices, power electronic devices and way other applications, because of their direct bandgap that can be tuned over a large range of the electromagnetic spectrum: from the far ultraviolet (6.2 eV) to infrared wavelengths (0.7 eV), as shown in Figure 2.1. This property is very useful for optoelectronic devices working in the UV to green range since there is no other inorganic semiconductor material that is as efficient for light generation. [11, 12]

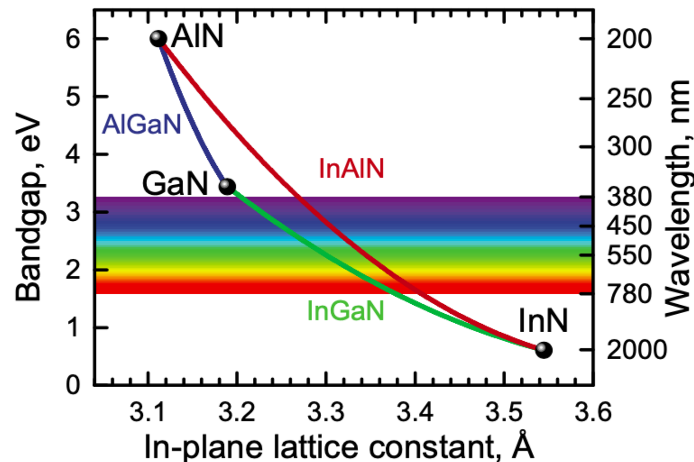

Figure 2.1: Bandgaps of wurtzite GaN, AlN and InN and their alloys versus their lattice constant at 300[K] [13]

The III-nitride materials can crystallize in 3 diffirent phases: wurzite, zincblende and rock-salt. But the wurtzite structure is thermodynamically stable under ambient conditions. This structure can be seen as two hexagonal closed-packed planes, with each a single type of atoms and with an AaBb stacking order. This hexagonal crystal structure induces a spontaneous and piezoelectric polarization which offers unique material properties. [11, 14, 15]

Electrical properties

A unique property of III-nitride is the high activation energy for acceptor doping, about 170 meV for Mg. This leads to a major challenge to achieve high hole concentrations using impurity doping. Usually Si is used for the n-doping at dopant concentrations up to 10^{19}cm^{-3}. Since the ionization energy for Si in GaN is low, the concentration of electrons can be approximated by the Si concentration. This is not the case anymore in AlGaN if the content of Al increases, since the ionization energy of the dopants also increases with the Al content. For p-doping, due to the high ionization energy of Mg because of the smaller effective mass of electrons compared to holes, the concentration of holes is limited to the order of 10^{18}cm^{-3}, with doping densities near 10^{20}cm^{-3}. In AlGaN, by increasing the Al content, it is getting more difficult to reach high hole concentration due to the higher ionization energy, just as for the n-doping. This high doping density causes a low hole mobility on the order of 10 $\frac{cm^2}{Vs}$, while the electron mobility is around 2000 $\frac{cm^2}{Vs}$. [16, 11, 15]

Optical properties

III-nitride semiconductors are direct bandgap materials. This bandgap can be tuned by alloying GaN and InN or AlN, as shown in Figure 2.1. The bandgap of a material is a very important parameter since it determines the transport and optical aspects of this semiconductor. GaN has a bandgap of around 3.4 eV, InN of 0.7 eV (near IR) and AlN of 6.2 eV (deep UV). So a wide range of the spectrum can be covered with teranry and quaternary alloys of InN, AlN and GaN. [11, 14]

Thermal properties

The chemical bonding within III-nitrides is very strong. This leads to high melting points and good resistance to high-current electrical degradation and radiation damage, which allows those devices to operate at high temperature and in hostile environments. [14]
Next to those properties, III-nitride binary compounds like AlN, GaN and InN have a higher thermal conductivity than ternary materials: AlGaN, InGaN and AlInN. This can be explained by the increase of the alloy scattering by acoustic phonons with the concentration of external atoms. They behave like additional scattering centers which reduce the thermal conductivity. In Figure 2.2, the thermal conductivity of AlGaN is shown. The equation leading to this graph will be explained in section 3.3.
The thermal conductivity will also depend on the deposition method and material quality as well as on the doping and thickness of the layers. [11] This will also be analysed in section 3.3

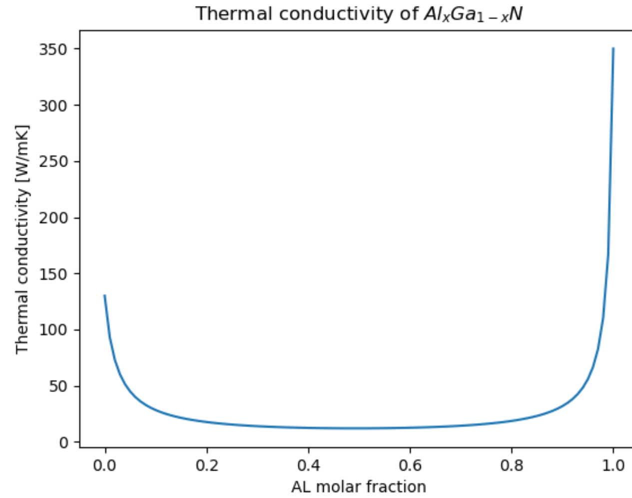

Figure 2.2: Computed thermal conductivity of AlGaN, using the material parameters from Adachi [17]

2.1.2 Fundamentals of vertical-cavity surface-emitting lasers

Basics of light generation

The photon emission of lasers is due to an electron that is giving energy up by transitioning from the conduction band to the valance band. For a light emitting diode (LED), the emission is spontaneous since each transition is an independent event. This is not the case for lasers, where the emission is stimulated. [16]

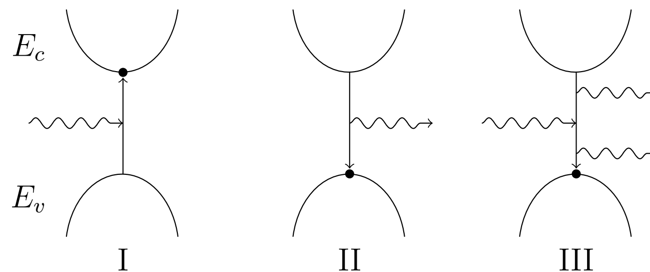

Figure 2.3: Schematic drawing of I: induced absorption, II: spontaneous emission, III: stimulated emission

When light interacts with a semiconductor device, there are three processes that can occur, as shown in Figure 2.3. In the first case an incident photon with sufficient energy is absorbed and an electron is elevated to a higher energy state. The opposite process can happen where the electron spontaneously transits back to the

lower energy state and a photon is emitted; this process is called the spontaneous emission. In the last case, if an incident photon is there at the same time as an electron in a higher energy state, a stimulated emission can occur, as predicted by Eistein in 1917 [18]. The photon will interact with the electron and induce a downward transition. This produces a photon. This process emits thus two photons, which are in phase, allowing the spectral output to be coherent. It is also interesting to note that the last process produces an optical gain or amplification. [16, 19]

The previous processes are all called radiative processes, they lead to light emission. On the contrary, non-radiative processes produces phonons or heating of the lattice. The main non-radiative processes are Auger and Shockley-Read-Hall recombination.

If N_c and N_v are the electron densities at the minimum of conduction band and maximum of the valance band respectively, N_c needs to be higher than N_v to reach optical amplification. This is not the case at thermal equilibrium where $N_c < N_v$ and thus the probability of induced absorption is the same as stimulated emission. For lasing to occur it is needed to reach population inversion. This can be done in two ways. Either by applying an external optical source (optical pumping) or by increasing the number of carriers by applying a forward bias voltage (electrical pumping). For optical pumping an external laser with shorter wavelength than the emission one is usually used as external source. In the case of electrical pumping, it is done through electrical contacts for current injection. The current path is then defined by current confinement strategies, such as the creation of an oxide aperture by lateral oxidation or ion implantation.

Different types of lasers

There exist different types of laser diodes and they can be technologically divided into two main groups: edge-emitting lasers (EELs) and VCSELs. Just like the name is saying, EELs are edge emitters, horizontally to the chip surface. The optical characterization of those devices can only be done after reflecting surfaces have been attached to the chip edges. This is not the case for VCSELs, which emit vertically to the surface. Since the mirror that is required for the laser cavity is already incorporated in the layer structure, optical characterization can already be done when the VCSEL is still on the wafer. [20]

The other main advantage of VCSELs over EELs is the relatively small size and vertical geometry that offers the possibility for high packing density. So the benefit of on-wafer testing and the high packing density make VCSELs more economical than EEL in a production environment. [21]
The many manufacturing challenges are the main drawbacks of the VCSEL structure.

A high-reflectivity mirror is needed and the cavity length is also very sensitive to variation.

Operating principle of VCSELS

The typical structure of a VCSEL is shown in Figure 2.4.

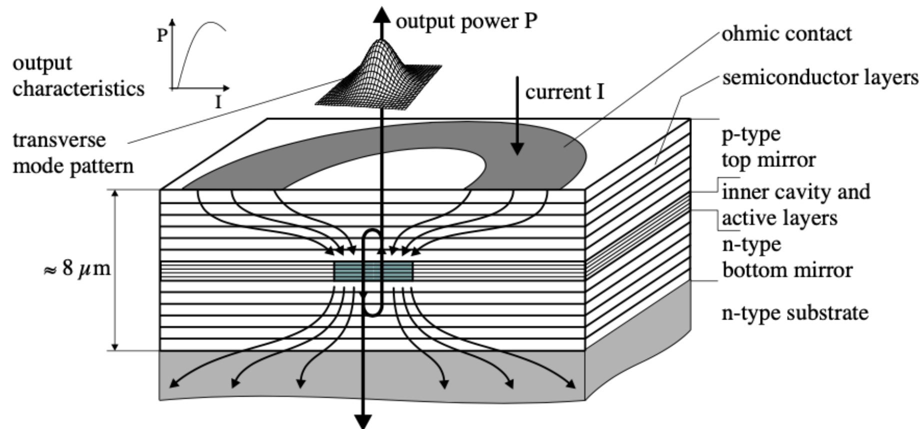

Figure 2.4: Schematic layer structure and operation principle of a VCSEL [22]

As explained, the laser action is based on stimulated emission, thus, confinement carriers and photons in the same space is the essence of lasers. The active layer consists of multiple quantum wells (MQWs) to provide the vertical confinement of the carriers within themselves. The oxide layers (e.g. SiO_2) allow for lateral confinement, both of light and carriers.[3]

As can be seen, the optical feedback is formed by an inner cavity that contains the active layers and they are surrounded by two mirrors that are parallel with the wafer plane. Due to the vertical geometry, the round-trip gain that amplifies the signal emitted from the MQWs is small. A high reflectivity of the mirrors is thus required to reduce the round-trip losses and so improve the optical gain.

The mirrors that are usually employed are distributed Bragg reflectors (DBRs), they are based on the concept of multiple reflections and constructive interference . Those mirrors allow to reach high reflectivity at specific wavelengths. The light will be emitted from the mirror that is less reflective; there are thus to types of VCSELs: top- and bottom-emitting VCSELs.

Optical waves will form standing wave patterns in the cavity. For the purpose of obtaining maximum gain, the active region needs to be placed at an optical antinode of the standing wave, position which corresponds to the maximum of the waves. While the lossy layers like the indium thin oxide (ITO), that is a current spreading layer, needs to be positioned at optical node. This helps to enhance the coupling between laser mode and active region and to reduce the threshold condition. [11, 22, 1]

The next points explains more in detail the most important parts of the VCSELs that will be useful for the understanding of future sections:

- **DBR**
  A DBR consists of a stack of an alternating sequence of high and low refractive index material with a thickness that corresponds to a quarter of the material target wavelength. By doing so, the partial reflection at each interface adds constructively. The electric field distributions and reflectivity spectra of these mirror can be calculated by the transfer matrix method described in subsection 5.1.1 The DBR that are used in VCSELs should exhibit a wide high-reflectivity band (stopband), high reflectivity in the stopband, and flat phase change on reflection. This can be achieved by choosing a high refractive index contrast of the two materials. To increase the reflectivity in the stopband, the number of pairs can be increased. [11][22][23][24]

  The reflectivity spectrum of this mirror is comb-shaped with a broad high reflectivity peak centered at a wavelength λ_{DBR}:

  $$\lambda_{DBR} = 2 \times (n_L t_L + n_H t_H) \tag{2.1}$$

  where n_L and n_H are the low and high refractive indexes with the thickness t_L and t_H respectively. In order to optimize the effect of the mirror, the λ_{DBR} must match with the target lasing wavlength λ_0. [24]

  The spacing between the different allowed cavity modes can be estimated by:

  $$\Delta\lambda_l \approx \frac{\lambda^2}{2L_{eff}\langle \bar{n}_{gr} \rangle} \tag{2.2}$$

  where $\langle \bar{n}_{gr} \rangle$ is the spatial average of the group index $\bar{n}_{gr} = \bar{n} - \frac{\mathrm{d}\bar{n}}{\mathrm{d}\lambda}$ and where L_{eff} is the total effective length of the cavity, that is calculated as the sum of the length of the inner cavity and the penetration depth of the field in the DBRs: $L_{eff} = L + l_{eff,t} + l_{eff,b}$, where L is the length of the inner cavity. The

new parameter l_{eff} has the meaning of an effective mirror length, considering the phase penetration depth of the incident wave into the Bragg reflector:

$$l_{eff} \approx \frac{\lambda_{DBR}}{4(n_H - n_L)} \tag{2.3}$$

A single longitudinal mode emission can be achieved by growing a thin inner cavity, leading to large spacing between the different resonant modes, so that only one cavity mode falls within the within the reflectivity curve of the DBR and the spectral gain bandwidth. [25, 22, 16]

- **Threshold gain and current**

  The amplification of light as it travels through the active region is represented by an optical material gain g. A higher gain is reached if the pumping is increased, leading to a higher stimulated emission rate. To be able to lase, the gain must compete with a couple of loss mechanisms: absorption loss, mirror loss and diffraction loss, represented in Figure 2.5.

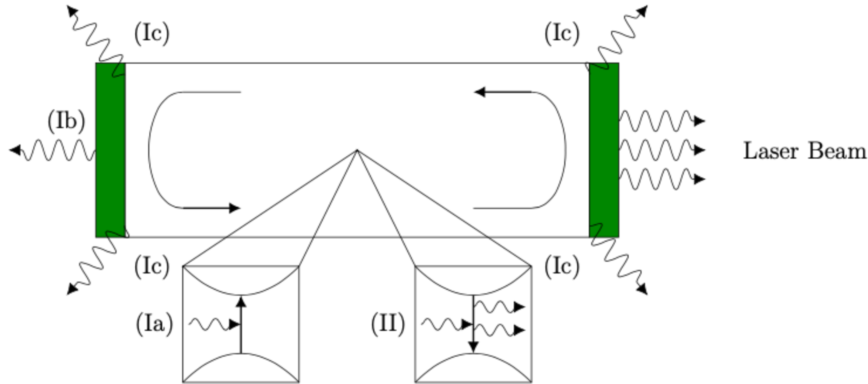

Figure 2.5: Schematic description of a typical laser optical cavity. The green sections represent semitransparent mirrors. The mirror on the right has lower reflectivity than the mirror on the left, hence a stronger beam is transmitted on the right hand side. The roman (I) correspond to the main types of optical losses: (Ia) Electromagnetic absorption, (Ib) Mirror losses, and (Ic) Diffraction losses. (II) is stimulated emission. [26]

The minimum gain required for a mode of the laser to reach threshold is called the threshold gain material g_{th}, this corresponds to the state where the material gain completely compensates the total loss, so that the electric field exactly replicates itself after one round trip in the cavity [27]:

$$\Gamma_{\text{active}}\, g_{th} = \alpha_{abs} + \alpha_m + \alpha_d \tag{2.4}$$

where α_{abs} is the absorption loss, α_m is the mirror loss, and α_d stands for the diffraction losses; where the gain and losses have the following unit: [1/cm]. Γ_{active} is the optical confinement factor that describes the portion of the total optical power that is confined within the active region of the cavity; it measures the overlap between the optical field and the active region. [26]

Knowing the threshold gain, the required threshold carrier density n_{th} depends on the chosen active material. The emission wavelength of a VCSEL is dictated by the resonator and not by the spectral position of the gain peak. For perfect alignment with the threshold current density follows as [22]:

$$j_{\text{th}} = \frac{q d_{\text{a}}}{\eta_I \tau_{\text{sp}}} n_{\text{th}} \tag{2.5}$$

where q is the elementary charge, d_a is the active region thickness and η_I is the carrier injection efficiency accounting for lateral leakage currents and carrier overflow over confining barriers. The last parameter in this equation is the spontaneous recombination lifetime τ_{sp} that can be expressed by [22]:

$$\frac{1}{\tau_{sp}(n)} = A + Bn + Cn^2 \tag{2.6}$$

with A, B and C coefficients expresses the non-radiative interface or surface recombination, radiative bimolecular recombination and Auger recombination, respectively.
The threshold current can now be calculated by multiplying the threshold current density by the active region area A_a:

$$I_{th} = j_{th} A_a = \frac{qV_a}{\eta_I \tau_{sp}} n_{th} = \frac{qV_a}{\eta_I}\left(A n_{th} + B n_{th}^2 + C n_{th}^3\right) \tag{2.7}$$

where the active volume V_a is the multiplication of the active area A_a and the active thickness d_a. The threshold current is directly proportional to the active region area, the small active region volumes allows thus really low threshold current, as will be seen in the analysis of the impact of the aperture on the temperature. However when the active diameter is reduced to below $\approx 4[\mu m]$ in oxide-confined VCSELs, increased diffraction and scattering losses as well as a decreased transverse confinement factor Γ_t lead to an increase of I_{th}. [22]

- **Output power and Quantum Efficiency** Above threshold, the output power lasing through the top or bottom mirror is linearly increasing with the driving current[22, 27]:

$$P_0 = \eta_{dt,b} \frac{\hbar\omega}{q} (I - I_{th}) \tag{2.8}$$

where $\eta_{dt,b}$ is the differential quantum efficiency defined as the fraction of injected electrons that produce coherent emission in the external beam. $\hbar\omega$ is the photon energy with $\hbar$ the reduced Planck's constant and ω the optical angular frequency.

The differential quantum efficiency can be computed by measuring the slope of the P-I curve, shown in Figure 2.6, in W/A above threshold, it needs then to be multiplied by $[\frac{q}{h\nu}]$ in C/J to get an empirical number of photons per electron equal to [27]:

$$\eta_d = \left[\frac{q}{hv}\right] \frac{dP_0}{dI} \cdot \quad (I > I_{th}) \tag{2.9}$$

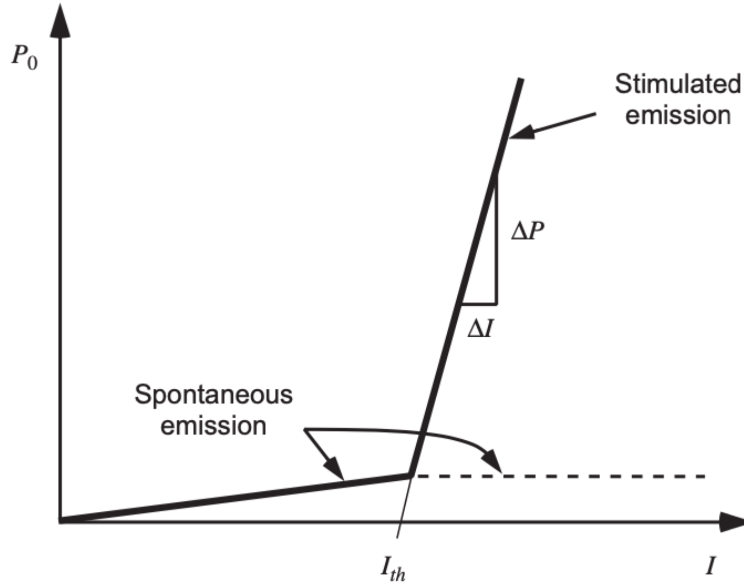

Figure 2.6: Output power versus driving current for a diode laser [27]

As shown in Figure 2.6, below threshold the generation of photons is dominated by the spontaneous emission; above threshold the stimulated emission is dominating and the spontaneous emission is fixed at its threshold value.

2.1.3 GaN based VCSELs and DBR

Basic structure of GaN VCSEL

A schematic view of an electrically injected GaN VCSEL is shown in Figure 2.7. The main difference with other VCSEL like GaAS-based VCSELs is the use of one or two dielectric DBRs. This can be explained by the lack of two near lattice-matched materials with high refractive index contrast. Dielectric DBRs are typically electrically insulating; lateral current injection through intra-cavity current spreading layers are thus mandatory. Due to the low electrical conductivity of p-GaN, transparent current spreading layers are used to inject the current in the multiple InGaN QWs. These layers needs to be thin and thus heavily doped, resulting in a trade-off between electrical impedance and optical absorptive loss. [2, 28]

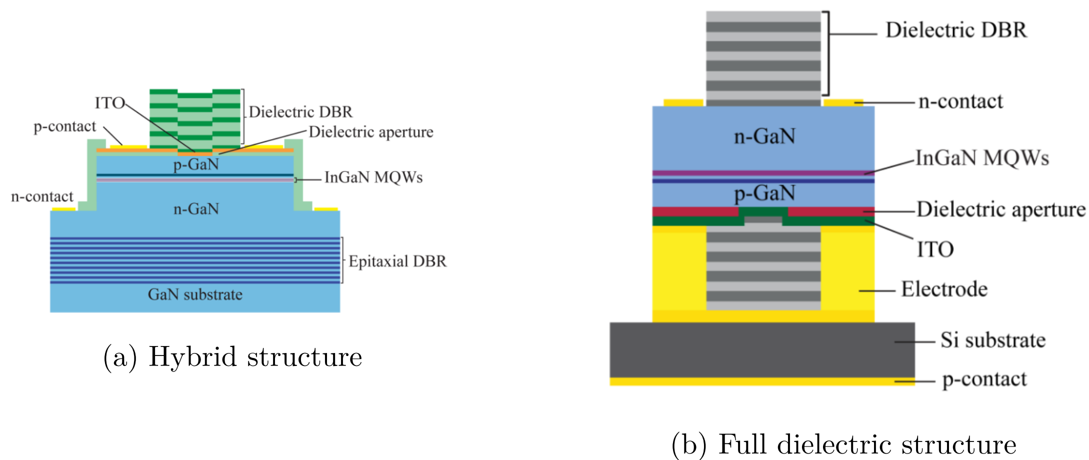

(a) Hybrid structure

(b) Full dielectric structure

Figure 2.7: A schematic view of a GaN-based VCSEL with 2.7a hybrid DBRs or 2.7b two dielectric DBRs [2]

Different types of DBR

As explained earlier, the DBR is a key building block of VCSELs. The success in epitaxial GaAs DBR mirrors has opened the way to the multiple communication and mobile applications. This is not the case for GaN-based blue VCSEL due to the many challenges (mechanical, optical and electrical) in preparing DBRs that are mass producible. The research of epitaxial DBRs started in the '90s and evolved from using AlGaN, AlN, to using lattice-matched AlInN with GaN. In parallel, dielectric DBRs have been studied since 2000 . [28]

As already explained dielectric DBR are insulating and requires lateral current injection through intra-cavity current spreading layers. This architecture leads to current crowding, large device footprint, and extra fabrication processes. Epitaxial semiconductor DBR mirrors offer good electrical conductivities and improved thermal conductivities over their dielectric counterpart. Conductive DBRs enable vertical current injection into the gain region of a VCSEL for best current uniformity and device impedance.

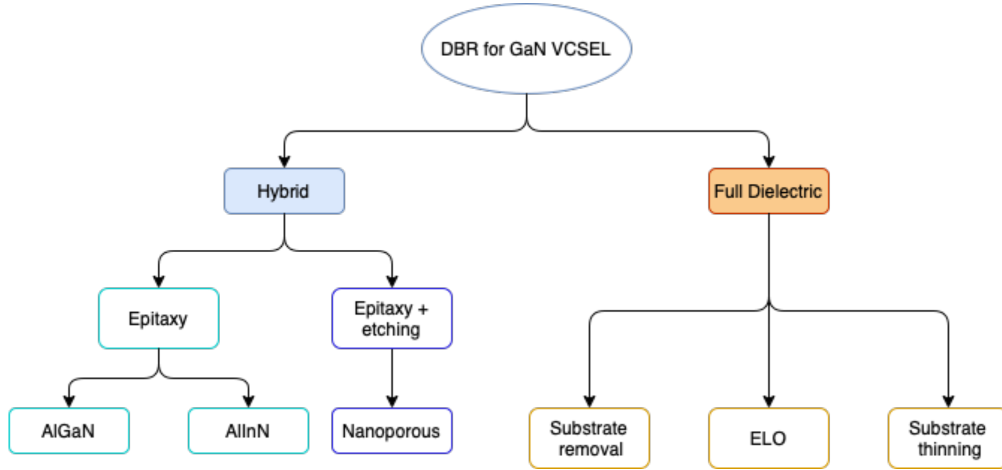

Figure 2.8: A chart depicting different approaches to prepare DBRs toward the fabrication of III-nitride VCSEL devices, modified from [28]

A review of the development of different DBRs in GaN VCSELs is shown in Figure 2.8. For the III-nitride VCSELs, it can be said that p-type III-nitride epitaxial DBRs is not producible in the near future so the types of III-nitride VCSEL are divided into either hybrid (dielectric-epitaxial) or all dielectric version:

Epitaxial DBR for GaN VCSELs

- **AlGaN**

  AlN can be a good material for an epitaxial DBR with GaN due to the high index contrast: 0.34. However a large lattice mismatch: 2.4% introduces an excessive tensile and compressive strain and stress around 7 kPa within the layers, which highly deteriorates the performances of this DBR. A solution to this is to introduce the AlGaN compound to reduce the strain but this implies a large number of pairs (> 50) due to the lower index contrast. [28, 1]

In 2008 National Chiao Tung University (NCTU) reported the continuous-wave operation at room temperature of an electrically injected GaN VCSEL, using a strain-engineered AlN/GaN DBR in combination with a top dielectric Ta_2O_5/SiO_2 DBR [29]

- **AlInN** The growth of AlInN has been challenging due to both the large mismatch between InN and AlN covalent bonds and due to the difference of growth conditions using MOCVD. Regardless of these difficulties, AlInN wih an 80% Al compound is very interesting due to its ability to be made completely lattice-matched to GaN. The typical growth of AlInN is very slow (<0.2 μm/h)[28]. In 2012 École Polytechnique Fédérale de Lausanne (EPFL) reported an electrically injected GaN VCSEL with a bottom AlInN/GaN DBR and a top TiO_2 /SiO_2 DBR. [30].

  In 2016, Meijo University demonstrated a VCSEL with conductive AlInN/-GaN DBRs with back-side contact, showing the feasibility of GaN-based VCSELs with vertical current injections through conducting DBRs [31]

Non-Epitaxial DBRs for GaN VCSELs

Dielectric DBRs have always been considered as the backup plan or even the only option, due to the complexity of the epitaxial DBRs as explained just before. There exists several methods to remove the substrates in order to deposit the bottom DBR mirror. Other innovative methods to encase the active region such as epitaxial lateral overgrowth (ELO) and substrate thinning, shows very promising results.[28]

- **Dielectric DBR through substrate removal**

  Nichia [32] and UCSB [10] demonstrated GaN VCSELs using a flip-chip method, this includes substrate removal; this can be accomplished by laser-induced liftoff (LLO) photoelectrochemical (PEC) etching of a sacrificial layer , as done by UCSB, wet/dry etching or chemo-mechanical polishing (CMP). Usually a polishing step is required to smooth the surface after the substrate removal.[28]

- **Non-Epitaxial DBRs through Epitaxial Lateral Overgrowth (ELO)**

  In 2015 Sony Corporation reported the use of ELO to fabricate double dielectric VCSELs without substrate removal. This technique was originally used to grow GaN over patterned dielectric mask region, this reduces the dislocations.[33] The limitation of this technique is the minimum thickness of the cavity and the increased diffraction loss for long planar VCSEL cavity (>1% per round).[28]

- **Non-Epitaxial DBRs through Substrate Thinning and Curved Dielectric Mirrors**

  Sony presented in 2018 another solution with dielectric mirrors using the concept of "external cavity" [34]; after thinning the substrate, a cuved mirror is coated on the substrate side. This implementation is easier than the other approaches presented before.

Nanoporous DBR

Air is the ultimate low-index material; innovative ways to include it in GaN DBR from epitaxial GaN structures have been proposed. The air-containing layers are typically done in a two-step process [28]:

- First through epitaxy of a “DBR structure”
- Next by selective etching through either chemical, electrochemical, photoelectrochemical, or thermal means.

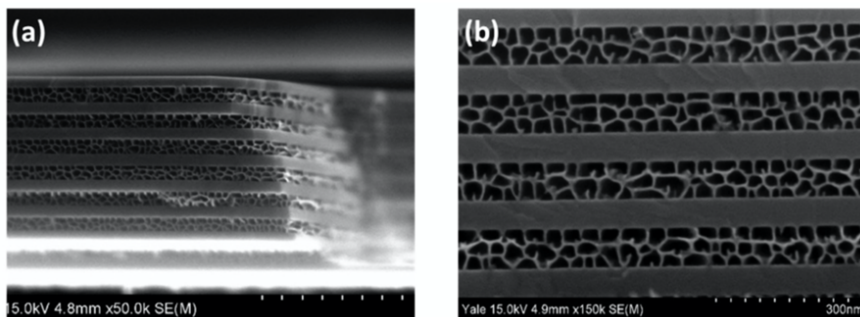

Figure 2.9: Cross-sectional SEM images of (a) a NP GaN/GaN DBR structure and (b) NP GaN/GaN DBR at a higher magnification [35]

A cross-sectional scanning electron microscopy (SEM) image of a porous GaN DBR is shown in Figure 2.9; The NP GaN have a porosity of 70% and an average pore size of 30 nm. As can be seen, the NP GaN has similar to foam or sponge-like texture, as it can be considered as a nano-composite of perfect single crystalline GaN filled with nanoscale, inter-connected tubes. [28]
Compared to the previous epitaxial DBR: AlGaN or AlInN, the epitaxy of n-GaN/n++GaN is straightforward. The other unique advantages of using this n-type doping profile to produce NP-GaN layers are:

1. A complete lattice matching to conventional GaN structures with negligible degradation in microstructure or morphology

2. A high tunability in the index of refractive index
3. The feasibility of electrical injection through n-type NP GaN layers

In 2019 the first electrically injected nitride VCSEL with an electrically insulating bottom porous DBR, made on m-plane GaN has been created, requiring intra-cavity injection. [36] In 2020, the first NP GaN c-plane VCSEL on conductive NP DBR which enables vertical current injection NP GaN VCSEL Design was presented by Elafandy et al. [37].
The main drawback of NP-GaN DBR is the limited thermal conductivity due to the reduced phonon mean free path. The thermal conductivity of NP material depends on the pore size. If it is close to the phonon mean free path at zero-porosity, it can be expected that the thermal conductivity will decrease significantly due to the phonon-pore scattering. [38]

2.2 Nanoporous DBR and VCSELs: fundamentals and advantages

2.2.1 Formation of porous GaN

Since III-nitride material system is highly chemically-inert, it makes the etching of GaN films via traditional wet-etching methods difficult. A review of the progress in porous nitrides is thus made in this section, focussing on the electrochemical and photoelectrochemical methods.
Other alternative ways to make porous nitrides are listed here:

- Large-area, free-standing and single-crystalline porous Gan membranes are prepared using a one-step high-temperature annealing technique. [39]
- Homoepitaxial nanoporous GaN layers are grown in a single step by CVD on non-porous GaN deposited on sapphire substrates [40]
- A new deposition formation was observed with a Mather-type Plasma Focus Device (MPFD) [41]
- Highly crystalline NP-GaN materials have been synthesized by the transformation of novel diamino tetrazine based mesoporous carbon nitride (MCN-4) having very high nitrogen content and GaCl3 through the unique reactive hard templating approach. [42]

Let us now focus on the use of electrochemical etching (ECE) and photoelectrochemical etching (PECE):
The basic set-up is shown in Figure 2.10. It consists of [43]:

- A nitride based sample to be porosified, connected as the anode.
- An inert counter electrode, connected as the cathode.
- An electrolyte, forming an ionic conduction path between the electrodes.
- An applied potential between the anode and cathode from a voltage or current source.
- For PECE, the sample is illuminated using a high energy UV lamp.

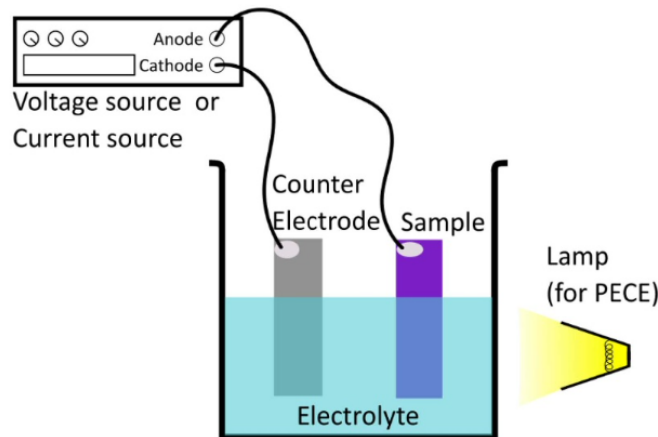

Figure 2.10: A schematic illustration of the basic electrochemical set-up for forming porous GaN [43]

The etching process has been described as a successive or cyclic four-step process [43, 44]:

1. First free-charge-carrier holes on the GaN surface in contact with the electrolyte are generated.
2. Next the GaN surface is oxidated by the holes.
3. Then the oxidization products are dissolved in the electrolyte.
4. Finally the products are transported away from the interface and reactants toward the interface.

This process is mainly controlled by the electric field that drives the injection of holes. The key parameters are thus the doping density and the applied potential. This will control the pore morphology.

The oxidation of GaN is an electrochemical reaction, driven by holes:

$$2\mathrm{GaN} + 6\mathrm{h}^{+} \rightarrow 2\mathrm{Ga}^{3+} + \mathrm{N}_2 \tag{2.10}$$

As can be seen in Equation 2.10, the process is driven by holes. In the case of PECE, the holes are created by the incident light that photogenerates electron-hole pairs that are then swept away by the electric field to the interface. In the case of ECE, carriers can be created in two ways: Zener tunneling or impact ionization by hot carriers. The band-to-band bending happens under high electric field and doping so that the bands will be tilted and that electron in the valence band can tunnel to the conduction band, leaving a hole behind. Impact ionization is happening at even higher applied potential since highly energetic electrons in the conduction band are needed to collide. Assessment of the potentials and doping density at which pores are formed assumes that band-to-band tunneling is the major source of free holes generation for the EC etching processes.[44, 43]

In an EC etching experiment, the two most important parameters are the anodic bias and conductivity of the layers. In Figure 2.11, the etching phase diagram is shown and can be divided into three regions [45, 43]:

1. Yellow region: Low applied bias or doping concentration: no chemical reactions happens and GaN stays intact.

2. Blue region: Increasing applied bias or doping concentration: electrostatic breakdown occurs with the injection of holes to certain localized hot spots, resulting in the formation of porous structures through localized dissolution intact.

3. Purple region: High applied bias or doping concentration: electropolishing (complete etching) takes place.

Pore size can be controlled by varying the potential or doping: at low potential near the no etching regimes, mesopores are formed for photonic applications (red dashed). While at higher potential near the electropolishing regime, macropores are generated for light scattering applications (blue dashed).

Generating layered porous structure can be done by either modulation the applied potential or by alternating the doped and non-intentionally doped layers:

- Griffin et al. [43] created layers of different porosity by modulating the applied potential. This is well established in porous silicon [46].

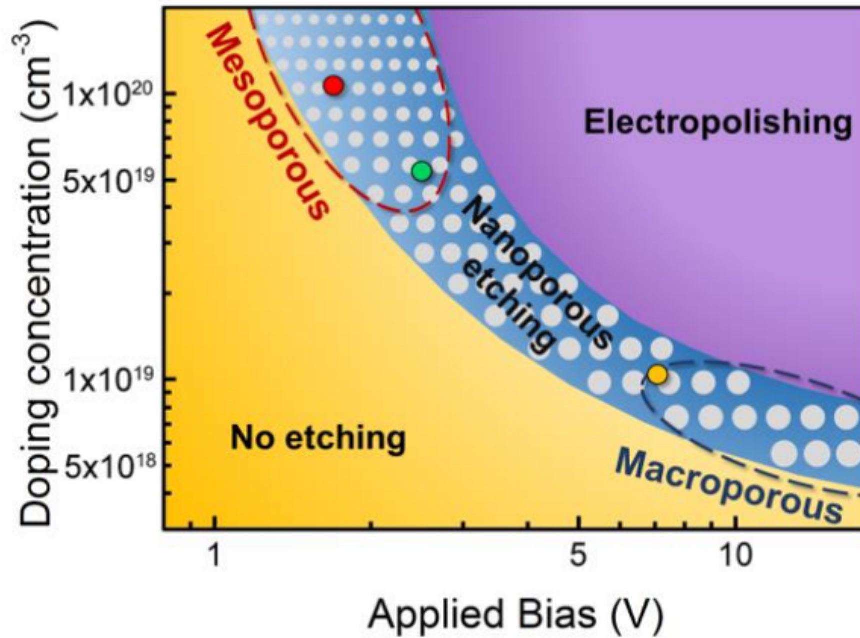

Figure 2.11: A processing phase diagram for EC etching [45]

- Unintentionally doped (UID) layers can be used as etch stop since the material is not conductive enough. Electrochemical etching can then create pores only in the doped layers. Layers of Si-doped and UID GaN are grown in an alternating structure, creating an NP-GaN/GaN DBR structure through ECE, as shown in Figure 2.9 by Zhang et al. [35]

2.2.2 Fabrication of NP DBR VCSELs

First an epitaxial structure consisting of 25 alternating n+GaN/GaN layers is grown to form the bottom DBR. Next the n-GaN cavity is grown, followed by the active region, EBL and p-GaN cavity, to create the epitaxial structure of the VCSEL cavity. Next the sample needs to be lithographically patterned with trenches to expose the sidewalls of the alternating layers. EC etching is than conducted by applying a bias (e.g. 1.65 V for 8 hours: 70% porosity[47]). Then a 15 μm diameter current aperture is defined using a 30 nm SiO_2 followed by a 30 nm sputtered and annealed ITO current spreading layer. Finally, a 40 nm HfO_2 spacer and a SiO_2/HfO_2 top dielectric DBR were deposited. [48]

The result of this fabrication process is shown in Figure 2.12:

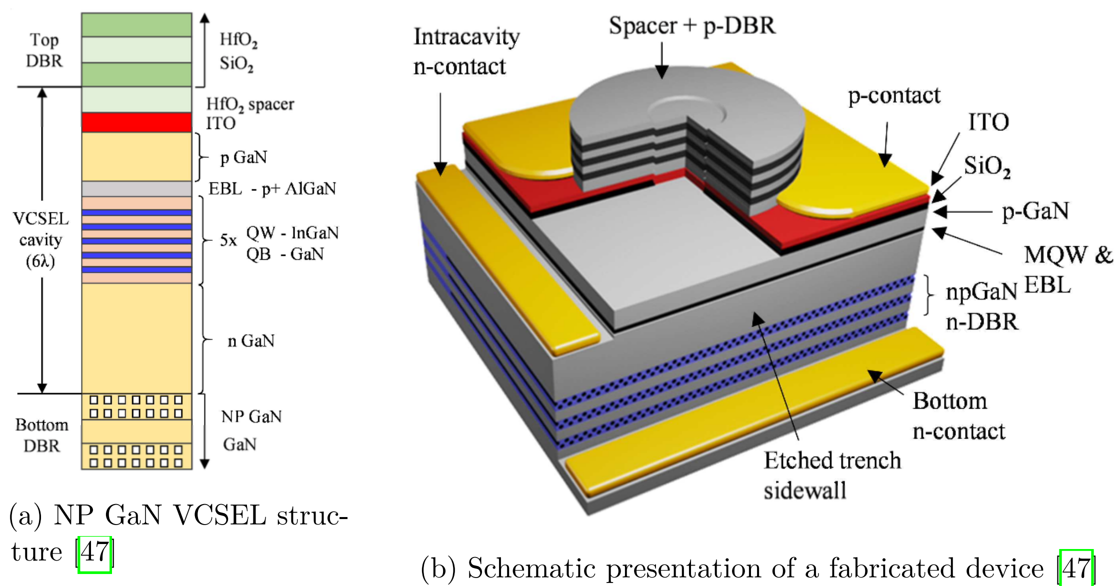

(a) NP GaN VCSEL structure [47]

(b) Schematic presentation of a fabricated device [47]

Figure 2.12: Structure of the NP VCSEL builded in [47]

2.2.3 Brief summary of NP DBR VCSELs

The advantages of NP GaN are multiple:

1. Provide unprecedented tunability in the index of refraction while maintaining perfectly lattice matched to GaN.[45]

2. NP-GaN also presents a nearly lossless character from scattering and excellent electrical conductivity.[45]

3. The feasibility of electrical injection through n-type NP GaN layers is thus possible due to electrical conductivity.

4. Compared to the epitaxial (AlN/GaN AlInN/GaN) and dielectric DBRs, offer a unique pathway for mass production.[48]

NP-GaN DBR seems to be a very good alternative to dielectric DBRs that are difficult to fabricate (substrate removal, lift-off ...) and they show the same peak reflectivity with a reasonable number of pairs compared to other epitaxial DBRs. However the main drawback of nanoporous layers is the limited thermal conductivity due to the phonon-pore scattering. This hinders the NP-GaN VCSELs to reach CW operation and has only be used under pulsed conditions:[48, 49]

2.3 Achieving Continuous-Wave (CW) Operation for NP GaN VCSELs

As already said, the NP GaN VCSEL has never been able to lase under CW operation. It could only lase under pulsed operation, which means that the VCSEL fails if it is turned on for more than a fraction of a millisecond. This is a main limitation preventing most practical applications.

For a laser, continuous-wave operation implies that it is continuously pumped and that it continuously emits light. But this operation mode can lead to too strong heating of the gain medium. The heating can be reduced by quasi-continuous-wave operation, where the pump power is only turned on for a limited time allowing to reach steady-state optical condition, reducing the thermal effects. The pulse width (PW) and pulse repetition rate (frequency) can be controlled so that the device is only turned on for a fraction of the time, as described by the duty cycle δ, which is defined as [50]:

$$\delta = PW \times f \tag{2.11}$$

Quasi-CW can be considered if the duty cycle is greater than 1%, while CW has a duty cycle of 100%. [51]

The following sections will resume the heat management in VCSELs and the effects of the heating on the performances of the device. The improvements to reduce the temperature in the existing GaN VCSELs and to reach CW will also be explained.

2.3.1 The heat equation

Heating is one of the main limiting mechanism of the performance of VCSELs, such as the drop of the optical gain, electrical conductivity and the increase of non-radiative recombinations. Furthermore, the thermal profile produces in the whole device a variation of refractive index leading to important consequences on the optical features. This is why it is important to analyse the heat mechanisms that causes the failure to lase under CW operation. This is done by solving the well known thermal conduction equation at steady state, since in the temperature dynamics is negligible, as the thermal time constants are at least one thousand times slower than all the other ones involved in VCSEL simulation [22, 15]:

$$\nabla \cdot (\kappa \nabla T) = -Q_{tot} \tag{2.12}$$

where ∇T is the temperature increase compared to the fixed temperature T_0 of the

heatsink. And κ is the thermal conductivity.

The heat sources in Q_{tot} are the [52, 53, 54, 55]

1. Joule effect
2. Optical absorption
3. Various non-radiative recombination mechanisms:

$$Q_{tot} = \sigma^{-1}\|\mathbf{J}\|^2 + \alpha W_{opt} + E_g R_{nr} + \Delta_{C/V} C_{n/p}^{cap} \tag{2.13}$$

Let us analyse each source more in detail:

1. The first term $\sigma^{-1}\|\mathbf{J}\|^2$ is due to the Joule heating dissipation mechanism. Where σ is the electrical conductivity that can be calculated by the product of the carrier density (n) and mobility (μ) for electrons and holes. And J is the injected current density. When a current flows into an impedance, the temperature rise is proportional to the square of the current.

2. The second term αW_{opt} is related to optical absorption mechanisms. Where the absorption coefficient α stands for the intra-band and free-carrier absorption phenomena distributed according to the 3D modal power density profile W_{opt}. [52]

3. The third term $E_g R_{nr}$ stands for the non-radiative phenomena, including Auger and Shockley-Read-Hall (SRH) recombination, where R_{nr} describes the non-radiative recombination rate and E_g is the energy bandgap of the material.

4. The last term $\Delta_{C/V} C_{n/p}^{cap}$ computes the contribution of carrier escape/capture by multiplying the conduction/valance band offset $Delta_{C/V}$ and the corresponding capture/escape rate $C_{n/p}$.

5. Thomson and Peltier effects are not included in this model since it is negligible compared to the other heat sources as reported by Ref. [52]

2.3.2 Effects of heating

VCSEL performance degrades at higher operating temperatures, which renders the CW operation impossible. The temperature increase in the VCSEL active region due to self-heating effects and non-radiative recombination induces a drastic decrease of the laser output performance. Three main temperature-induced effects are listed here:

1. The threshold current density increases with temperature. This is related to the Auger recombination and the vertical carrier leakage over the barriers.[56, 57] This can be observed by measuring the light-output power versus the driving current at various stage temperature[50, 27]
2. The output power is reduced with the increasing temperature caused by self-heating. This is called the thermal rollover.[58] It is shown in Ref. [59].
3. Misalignment of the cavity Fabry-Perot resonance wavelengths with the peak gain wavelength. Caused by the short optical resonator, the emission wavelength λ of a VCSEL is determined by the cavity resonance and not by the gain peak. However, with increasing temperature both the cavity resonance wavelength and the gain peak wavelength experience a red shift at different rates, leading to a detuning between these two wavelengths limiting the VCSEL output performances. [50, 22, 25]

Let us continue with a more detailed analysis of each effect and its dependence on the increasing temperature:

Threshold current density

As explained in subsection 2.1.2, the threshold current density is the nominal value of injected current that is necessary to generated lasing. Above threshold, inversion of the carrier population happens and stimulation recombination dominates over spontaneous recombination.

The temperature dependence of the threshold current density can be found by analysing the temperature dependence of Equation 2.7. By considering that around threshold the dominating recombination mechanism is the spontaneous recombination, Equation 2.7 can be expressed by the following equation for the carrier density at threshold [27]:

$$I_{th} \simeq \frac{qV_a}{\eta_I} B n_{th}^2 = \frac{qV_a}{\eta_I} B \left(N_{tr} e^{\frac{\langle \alpha_i \rangle \alpha_m}{\Gamma g_0}} \right)^2 \tag{2.14}$$

where N_{tr} is the transparency carrier density $\propto$ T , $g_0 \propto \frac{1}{T}$ and $\alpha_i \propto$ T. It can thus be deduced that the threshold current density is exponentially increasing with temperature. Other recombination mechanisms like Auger or SRH recombination or carrier leakage, will further enhance the temperature increase. The non-radiative processes are temperature-dependent via the increased carrier density necessary to balance the optical loss [23]. The increased carrier leakage can be explained by the fact that an increasing temperature raises the vertical leakage of carriers, allowing

trapped electrons in the quantum well (QW) to leak from the potential well to the contact layers of the cavity where the recombination of carriers is not contributing to the output light power. This means that the amount of carriers injected in the cavity needs to be higher to achieve the same carrier population in the QW; the threshold current density is thus raised by the temperature. [25, 60]

Thermal rollover

This mechanism is defined as the saturation of the output power with increasing bias current above threshold or increasing ambient temperature. The deviation from the linear increase of light output power with the driving current is caused by

1. Higher carrier densities to maintain the threshold gain
2. Carrier and current leakage effects: as explained before, the carrier leakage out of the active region leads to a lower injection efficiency
3. Increased non-radiative recombination

Thermal rollover is one of the main limitations of nitride based emitters due to the non-optimized dissipation of heat in the VCSEL. [25, 27, 58]

Wavelength shift

The only observable quantity linked to temperature, even though not directly, is the emission wavelength that is mainly governed by the cavity resonance and not by the gain peak as in EEL. The thermal wavelength shift is thus governed by changes of the average refractive index in the short-resonator cavity. On the other hand, the active region show a shift of the peak wavelength due to the bandgap shrinkage; at higher temperature, the emission of light from the QW will then occur at lower energies which corresponds to higher wavelengths. This shift is faster than the resonance wavelength shift, causing a misalignment between both wavelengths. This reduces the output optical power drastically [61, 53, 22, 50]

2.3.3 Thermal management

It is interesting to analyse how this thermal problem has been solved. But before doing so, it is important to understand how to compare different VCSELs. This can be done by means of the thermal resistance.

Thermal resistance

The concept of thermal resistance R_{th} is frequently used to determine the extent of device heating. It is defined as the ratio of the mean temperature increase in the active region to the total dissipated thermal power in the device:

$$R_{th} = \frac{\Delta T}{P_{diss}}\left[\frac{^{\circ}C}{W}\right] \tag{2.15}$$

This is very similar to the electrical resistance; it does not only depend on the material properties but also on the geometry. The advantage of using this value is the thermal characterization of the device by experimental measurement:

$$R_{th} = \frac{\frac{\Delta\lambda}{\Delta P_{diss}}}{\frac{\Delta\lambda}{\Delta T}} \tag{2.16}$$

Where $\frac{\Delta\lambda}{\Delta P_{diss}}$ is the measurement of the wavelength shift with the consumed power and $\frac{\Delta\lambda}{\Delta T}$ with varying heat-sink temperature. Usually the measure is done at pulsed operation to avoid heating. [15, 22, 24]

It is important to notice that even though this parameter seems very convenient to compare thermal properties of various devices, it can sometimes be misleading [62]: for example a device with a very poor electrical contact between the device chip and the heat sink. The heat generated at the interface between the heat sink and laser would be very efficiently extracted by the conductive heat sink, so its influence on the active-region heating would be relatively small although the generated heat near the heat sink would still contribute to the total heat source P_{diss}. This device would thus have a lower thermal resistance than a well mounted laser with a low electrical resistance contact. The thermal properties of devices should be used very carefully. [24]

Thermal management in the literature

Sarzala et al. [63] tried to analyse the influence of various bottom DBR designs on the thermal properties of blue GaN VCSELs. They first analysed the lattice-matched AlInN/GaN DBRs. As expected they concluded that the large number of DBR layers and the low thermal conductivity of AlInN leads to a high thermal resistance of the device: 3480 W/mK.

They then explored another epitaxial DBR: AlN/GaN DBR since it has attractive thermal properties. However, due to the lattice constant mismatch between the GaN and AlN, it cannot be implemented. A small-period superlattice layer is thus inserted between every few DBR pair to decrease the strain, which reduces the

density of crystal defects in GaN/AlN DBRs. This improves the thermal resistance of the device: 2140 W/mK.

The third bottom DBR to be analysed is the dielectric SiO_2/Ta_2O_5, it has a very high power reflectance but since it is an insulator, it makes the current injection challenging, as explained before. The thermal resistance of this device is very high: 5279 W/mK. To improve this, gold metal channels in the form of rings were proposed to allow the heat flux to bypass the bottom dielectric DBR. By doing so, the thermal impedance was reduced to 2613 W/mK. This is of the same order of magnitude as the VCSEL with SL AlN/GaN DBRs.

Another research group of Xiamen University compared the thermal characteristics of GaN-based VCSELs [9]. They analysed the impact of the cavity, mesa size and bottom DBR size. They reported that a thicker cavity improves the thermal dissipation and that the impact is even more pronounced for structures with a bottom DBR that has a low thermal conductivity. The same was noticed by Sarzala [63]. Next the effect of the mesa size was analysed and it seems that a larger mesa size helps heat dissipation, reducing the thermal resistance of the VCSEL. Finally the increase of the size of the bottom DBR is said to increase the thermal resistance.

Mishkat-Ul-Masabih and Leonard [8] investigated the effects of the aperture diameter and cladding layers thicknesses. They report that the thermal resistance decreases as the aperture size increases. They also proposed to increase the cavity length to reduce the thermal impedance. A larger cavity volume enables the heat to disperse throughout the structure rather than being concentrated near the active region.

Kuramoto et al. reached CW and followed the trend to increase the cavity length from 5 to 10 λ. This allowed to reduce the thermal resistance from 1100 °C/W to 710 °C/W.[64]

Forman et al. followed the same trend with a cavity of 23 λ. They also increased the thin metal contact that conformed around the bottom DBR and was a bottleneck for the heat flow. By doing so, they achieved CW operation and a thermal impedance of 1400 °C/W.[65]

NCTU conceived a GaN VCSEL capable of high-temperature operation by using epitaxial lateral overgrowth on prepatterned dielectric DBRs on a GaN template. And the patterned bottom DBR is recessed in the bonding metal to improve the heat conduction. Those metal paths are 20 μm thick to reduce the thermal

impedance. [60]

This thermal analysis has never been performed for NP GaN-based VCSELs. The same trends are expected for the cavity length and the aperture. But the impact of the porosity on the thermal resistance has never been investigated and could be of great interest for the thermal management of porous DBRs.

Chapter 3

Simulations: Thermal modeling of VCSELs in COMSOL

Contents

3.1 COMSOL thermal application **31**

3.2 Literature example **32**

3.3 Hypothesis **33**

3.3.1 Thermal conductivity and refractive index 33

3.3.2 Effective DBR layer 33

3.3.3 Steady-state simulation 34

3.3.4 Heat exchange and sources 35

3.4 Device configuration and dimensions **36**

3.5 Material properties **39**

3.6 Boundary conditions **40**

3.6.1 Thermal boundaries 40

3.6.2 Axial symmetry 40

3.7 Meshing principles **41**

3.8 Simulation results and flux analysis **42**

3.9 Validation with already working VCSELs **47**

Overview

This chapter describes how the nanoporous VCSEL has been modelled in COMSOL. It starts with an example of the literature to understand the model and analyse the hypotheses that need to be made. Next the device is configured in COMSOL and the dimensions and materials properties are listed. The mesh is then simulated and the basic simulation results are analysed afterwards. The final model is ultimately validated with existing values in the literature. Everyone following all the steps of this chapter will be able to make the same model on their own.

The thermal simulation of the nanoporous VCSEL has been performed using the heat transfer module in COMSOL Multiphysics. The heat flow in the device and the maximum temperature achieved in the active region are the main results that will be analysed in the following sections.

A simulation in COMSOL always follows the same pattern:

1. Define the geometry
2. Implement the physics: equations, material properties, boundary conditions ...
3. Generate a mesh
4. Run the simulation
5. Post-process of the simulation results

3.1 COMSOL thermal application

The Heat Transfer module in COMSOL allows to model the VCSEL thermal problem. The Heat Transfer in Solids module solves the following equation [66]:

$$\rho C_p(\frac{\delta T}{\delta t} + \mathbf{u}_{trans} \cdot \nabla T) + \nabla \cdot \mathbf{q} = Q + Q_{ted} \tag{3.1}$$

$$\mathbf{q} = -k\nabla T \tag{3.2}$$

$$Q_{ted} = -\alpha T : \frac{\mathrm{d}S}{\mathrm{d}t} \tag{3.3}$$

The different quantities involved here are recalled below:

- ρ is the density $[\frac{kg}{m^3}]$
- C_p is the specific heat capacity at constant stress $[\frac{J}{kg \cdot K}]$
- T is the absolute temperature [K]
- $\mathbf{u}_{trans}$ is the velocity vector of translational motion $[\frac{m}{s}]$
- $\mathbf{q}$ is the heat flux $[\frac{W}{m^2}]$
- α is the coefficient of thermal expansion $[\frac{1}{K}]$
- S is the second Piola-Kirchhoff stress tensor [Pa]

- Q contains the additional heat sources $[\frac{W}{m^3}]$
- Q_{ted} is the thermoelastic damping
- k is the thermal conductivity $[\frac{W}{mK}]$

For steady-state problems, the temperature does not change with time and the terms with time derivatives disappear.
By excluding the viscous heating and pressure work terms, the governing equation becomes:

$$\rho C_p \frac{\delta T}{\delta t} + \nabla \cdot (-k \nabla T) = Q \tag{3.4}$$

3.2 Literature example

Before starting to simulate the nanoporous device, an example from the literature will be simulated to verify the process explained previously.
The VCSEL that was simulated was from the University of California Santa Barbara (UCSB), they managed to reach CW operation. The same 7λ VCSEL structure was modelled with an input power of 0.1 W. The same thermal conductivity values were used as the one listed in the paper [10]. The results of the simulation is shown in Figure 3.1a. This is in good agreement with what is reported by Forman et al. [10].

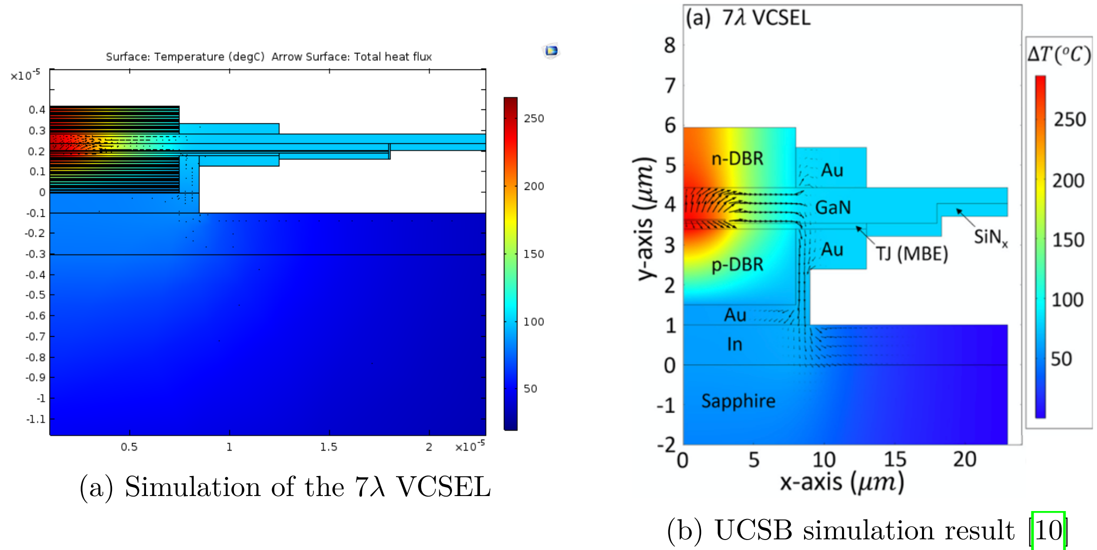

(a) Simulation of the 7λ VCSEL

(b) UCSB simulation result [10]

Figure 3.1: Comparison between the COMSOL simulation and the results of UCSB

The model simulated an active region temperature of 267 °C, while the reported temperature in the paper is 270 °C.

Now that the process is well understood, the same steps will be followed to model the NP VCSEL.

3.3 Hypothesis

Some hypotheses have been made to simplify the computations. They are all listed and explained in this subsection:

3.3.1 Thermal conductivity and refractive index

- Impact of the temperature: The thermal conductivity and refractive index of a material changes with temperature. But in this analysis we assume that it stays constant because the total heat power is kept low enough to neglect the dependency. The same has been done by other groups: [67, 9]. The impact of temperature on the refractive index will be taken into account in chapter 5
- Impact of the doping on GaN: The intrinsic thermal conductivity of GaN is above 200 W/mK. However, in real samples, the dislocation and size effect affect the lattice thermal conductivity seriously. A mediate value of 130 W/mK has thus been chosen. It has also been shown that size effects are more dominant than free carrier concentration on the thermal conductivity. The impact of the doping is thus neglected since it has small influence below 10^{20} cm^{-3}. [68]
- Alloys: The following formula has been used to compute the thermal conductivity of ternary alloys $A_xB_{1-x}C$:

$$\frac{1}{k(x)} = \frac{x}{k_{AB}} + \frac{1-x}{k_{AC}} + x(1-x)C_{ABC} \tag{3.5}$$

  where k_{AB} and k_{AC} stands for the thermal conductivity of the binary materials. C_{ABC} is the bowing parameter that allows to include the effect for alloy scattering. [17, 69]

3.3.2 Effective DBR layer

To simplify the complex VCSEL structures, the DBR layers can be replaced by an average material. This limits the high number of mesh points and demands less simulation time and memory. This approach has been used by multiple groups: [9,

70, 25, 71, 72, 8].

DBR layers are multilayers materials with different thicknesses and thermal conductivities, there is thus an anisotropic behaviour: $\kappa_1 \neq \kappa_2$. This can be taken into account by employing the model of serial and parallel thermal resistivity [67, 73]:

$$\kappa_r = \frac{d_1\kappa_1 + d_2\kappa_2}{d_1 + d_2} \tag{3.6}$$

$$\kappa_v = \frac{d_1 + d_2}{\frac{d_1}{\kappa_1} + \frac{d_2}{\kappa_2}} \tag{3.7}$$

where κ_1, κ_2 and d_1, d_2 are the thermal conductivity and the thickness of the alternating layers respectively.

It is clear from Equation 3.6 that the heat conduction is stronger in the radial direction than in the vertical direction. This can be explained by the reduction of the phonon mean free path by the thin layers boundaries [67] and also by the fact that multilayer stacks have a higher scattering by the interface phonons due to the thermal resistance at the interface between each layer [9].

The effective thermal conductivity of the QW was also taken into account. Otherwise an isotropic $\kappa = \kappa_v = \kappa_l$ is assumed for all other layers.

Since the analysis of the temperature in the active region and in the porous DBR is very important for the analysis of the thermal management, the QW and DBR were not replaced by an average material like it is usually done. The multilayers were all designed in COMSOL but the anisotropic thermal conductivity was computed and used for those layers, they are listed in Table 3.3.

3.3.3 Steady-state simulation

To analyse the heat flow and the evolution of the temperature with time, a time-dependent analysis is performed. The temperature that is reached in the active region after a few milliseconds corresponds to the temperature that is simulated by the stationary study, which is normal for a CW operation. This is depicted in Figure 3.2, where the temperature that is reached in the active region after 10 [ms] is 110 °C. This is the same value as the one that is computed by a steady-state study as shown in Figure 3.5

To analyse the impact of each parameter, a stationary study will be done to reduce the computation time, since only the final temperature in the cavity will be of

interest.

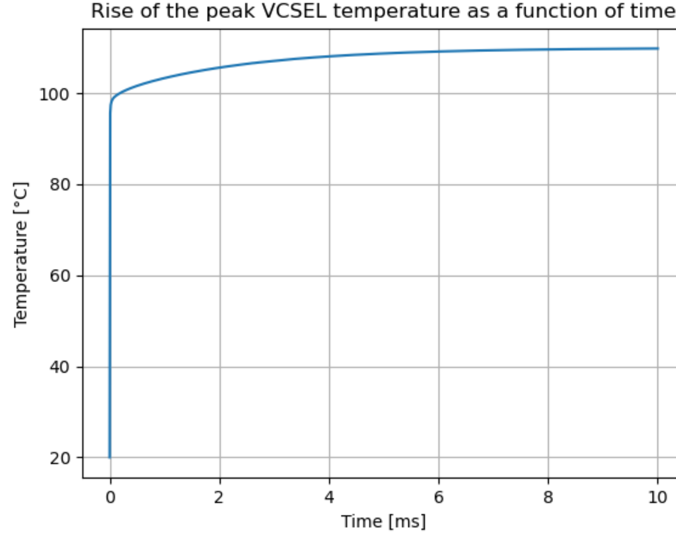

Figure 3.2: Evolution of the temperature in the active region with time

3.3.4 Heat exchange and sources

- Heat exchange with the outside: The heat produced in the active region is extracted out of the device by two means: conduction through the substrate and to the air by convection and radiation through the surface and edge wall. As has been reported by Lee et al. [71], the heat is mainly released by conduction and so convection and radiation are assumed negligible. [9, 72] This can be explained by the low heat transfer coefficient between the device and stationary air.[74]

- Heat sources: The heat power that is injected is estimated as the product of the injected current and the turn-on voltage:

$$P_{diss} = V_{on} \times (j_{th} \times (\frac{\text{aperture}}{2})^2) \tag{3.8}$$

This power is assumed to be generated within the active region since the wall-plug efficiency of GaN VCSEL is usually less than 3%, meaning that all the injected electrical power can be considered as being converted into heat. We can thus neglect the optical re-absorption, spontaneous emission

and lasing. The assumption is thus made that the heat is produced by non-radiative recombination in the active region and by the free carrier absorption of photons.[9, 67, 57] Joule heating is a heat sources that is not focussed in the active region but in the p-GaN, the small thickness of this layer compared to the n-GaN layer, allows to make the assumption that all the heat sources are lumped into a single source placed at the active region. [9, 53]

3.4 Device configuration and dimensions

The structure explained in subsection 2.2.2 has been configured in COMSOL. Since the VCSEL structure is symmetric around the z-axis, the axis that is perpendicular to the emission surface, the device is simulated in a 2D axisymmetric geometry. This means that a 2D section of the VCSEL is build and it is rotated around the z-axis to build the whole 3D structure. This allows to reduce the computational time.
From now on, the input coordinates for the geometry will be cylindrical, centered at the origin of the bottom DBR.

The NP geometry was constructed from scratch in the COMSOL desktop, based on Figure 3.3a, which is a sketch of the simplified VCSEL geometry. The thickness and radius of each layer is defined in a set of global parameters. Those parameters can be easily adjusted when it is required. A list of all the important parameters are presented in the following Tables: 3.1 and 3.2.

The result of the design in COMSOL is shown Figure 3.3b. The figured is zoomed around the active region to have a better understanding of the most important layers of the device.

The DBRs and the active region that consists of a few QW, are both structures that are composed of a lot of alternating layers. This can be easily constructed in COMSOL with the Parts section of COMSOL that can be found in the Geometry toolbar. Once the part is created, an array of N pairs can be generated, creating the intended DBR or active region.

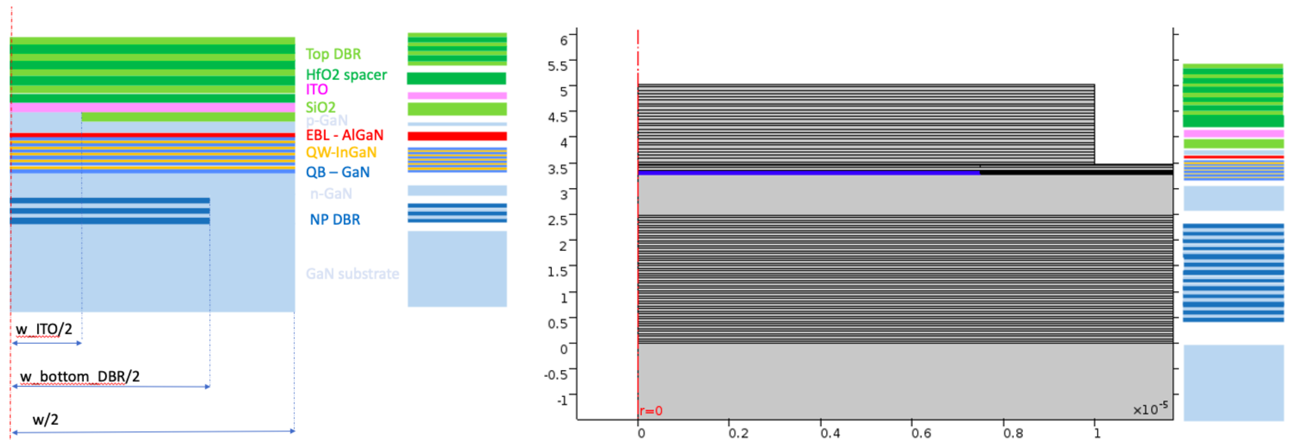

(a) Sketch of the VCSEL structure that has been simulated in COMSOL

(b) Zoom of the builded structure in COMSOL

Figure 3.3: Device configuration in COMSOL

Table 3.1: List of general parameters

Parameter	Expression	Description
λ	434 [nm]	Wavelength
n_HfO2	2.11	Refractive index HfO_2
n_SiO2	1.4668	Refractive index SiO_2 at 434[nm]
n_GaN	2.5063	Refractive index GaN at 434[nm]
n_ITO	2.07	Refractive index of ITO at 434[nm]
por	0.4	Porosity of the NP layers in the bottom DBR
n_NP	$\sqrt{(1-por)n_GaN^2+por}$	Refractive index of the NP layers
V	5.4 [V]	Turn-on voltage
j_{th}	$10\ [\frac{kA}{cm^2}]$	Threshold current density
I	$j_{th} \times (aperture/2)^2 \times \pi$	Injected current
P_diss	$V \times I$	Total dissipated power
V_active	$(\frac{aperture}{2})^2\pi(t_QWB \times N_QW)$	Avtive region volume
P_dens	$\frac{P_diss}{V_active}$	Power density
cycle_width	200	Pulse width in nanoseconds
duty_cycle	0.004	Duty cycle of the pulse

Table 3.2: List of geometrical parameters

Vertical parameters		
Parameter	Expression [nm]	Description
t_HfO2_DBR	$\frac{\lambda}{4n_\mathrm{HfO2}}$	Thickness of HfO2 DBR layer
t_SiO2_DBR	$\frac{\lambda}{4n_\mathrm{SiO2}}$	Thickness of SiO2 DBR layer
N_top_DBR	12	Number of pairs of the top DBR
t_GaN_DBR	$\frac{\lambda}{4n_\mathrm{GaN}}$	Thickness of GaN DBR layer
t_NP_DBR	$\frac{\lambda}{4n_\mathrm{NP}}$	Thickness of NP GaN DBR layer
N_bottom_DBR	25	Number of pairs of the bottom DBR
t_QW	3	Thickness of QW in the active region
t_QB	7	Thickness of quantum barrier (QB) in the active region
N_QW	5	Number of pairs of the active region
t_QWB	t_QW + t_QB	Thickness of a pair in the active region
t_GaN_substrate	100 [um]	Thickness of the GaN substrate
t_nGaN	806 - (6-N_cavity)$\frac{\lambda}{4\times n_GaN}$	Thickness of the n-GaN layer in the cavity
N_cavity	6	Number λ in the cavity
t_EBL	12	Thickness of the EBL
t_pGaN	60	Thickness of the p-GaN layer in the cavity
t_contact	15	Thickness of the contact layer
t_ITO	30	Thickness of the ITO layer
t_SiO2	30	Thickness of the SiO2 layer
t_spacer	40	Thickness of the HfO2 spacer layer
Radial parameters		
Parameter	Expression [um]	Description
w	200	Diameter of the whole structure
w_bottom_DBR	200	Diameter of the bottom DBR
w_ITO	15	Diameter of the ITO
aperture	15	Diameter of the aperture
w_mesa	20	Diameter of the mesa

3.5 Material properties

For the computation in COMSOL, only the thermal conductivity of each material is needed. However, the refractive index of the materials is also important since it will determine the thickness of the DBR layers and will be important to compute the resonance wavelength shift in section 5.1. The refractive index has been chosen at the resonance wavelength of the VCSEL: 434 nm.

The following table lists the properties of each material:

Layer	Material	Thermal conductivity $[\frac{W}{mK}]$	refractive index [/]
Top DBR	HfO2	$\kappa_r = 1.225$	1.9247[75]
	SiO2	$\kappa_v = 1.222$	1.4668[75]
Spacer	HfO2	1.2	1.9247[75]
ITO	indium thin oxide	3.95 [76]	2.07 [77]
Contact layer	p++GaN	130	2.5063[75]
Top p-GaN	p-GaN	130	2.5063[75]
EBL	p - $Al_{0.2}Ga_{0.8}N$	17.62	2.46 [78]
Active region	InGaN	$\kappa_r = 103.8$	2.57 [79]
	GaN	$\kappa_v = 73.4$	2.5063 [75]
Bottom n-GaN	n-Gan	130	2.5063[75]
Bottom DBR	GaN ([Si]: $5 \times 10^{18} cm^{-3}$)	$\kappa_r = 61.19$	2.5063 [75]
	NP GaN ([Ge]: $6 \times 10^{19} cm^{-3}$)	$\kappa_v = 8.91$	2.0418

Table 3.3: Material properties of each layer

As explained in the hypotheses (section 3.3), the thermal conductivity of doped GaN is assumed to be constant. The thermal conductivity of the DBR and active layers followed Equation 3.6.

The equation of the thermal conductivity of ternary alloys is explained in the hypothesis (Equation 3.5). The plot of $Al_xGa_{1-x}N$ is shown in Figure 2.2. The thermal conductivity at 0.2 molar fraction is 17.62 [W/mK].

Hafnium dioxide has a high refractive index (1.85–2.1) and a low absorption coefficient from UV to the mid-IR. [80] The thermal conductivity of this material is however strongly dependent on the thin-film thickness. The thermal conductivity

is set to 1.2 [W/mK] to obtain the most realistic results, as explained in [25].

For the porous layer in the bottom DBR, the following equations were used to compute the thermal conductivity and refractive index [81, 76]:

$$\kappa_{eff} = \kappa_0 \frac{1-\phi}{1+\phi} \frac{1}{1+\frac{l_0}{D}} \tag{3.9}$$

$$n_{eff} = \sqrt{(1-\phi) n_{GaN}^2 + \phi n_{air}^2} \tag{3.10}$$

where ϕ is the porosity, D the wall thickness and l_0 is the phonon mean free path, and a value of 100nm is used according to the supplemental materials of Ref. [76]. In Equation 3.9, the size effect is taken into account with $\frac{1}{1+\frac{l_0}{D}}$ to assess the impact of the phonon-pore scattering. [38, 76]

The thermal conductivity of porous medium is thus strongly dependent on the porosity and dimension of the nanopores [76]:

- If the wall thickness D is comparable to the phonon mean free path, the thermal conductivity will decrease due to the scattering.
- If the porosity increases, the conductivity will decrease due to the reduced effective medium.

3.6 Boundary conditions

3.6.1 Thermal boundaries

As explained in the hypothesis, radiation and convection are negligible. The following boundaries have thus been assumed to be:

- An initial temperature of 20 °C is set as initial condition in the whole simulation domain.
- The bottom of the substrate is forced at 20 °C.
- All the other boundaries of the device are thermally insulated.

3.6.2 Axial symmetry

Since the device is axisymmetric, the vertical centered axis (r = 0), also called the optical axis, is used as rotation axe to create the device.

3.7 Meshing principles

COMSOL software gives the user multiple options of mesh element types and meshing techniques. The default-option proposed by the software was used: the free-triangular mesh. The highest accuracy of solution is wanted in critical areas (in this case: active region and bottom DBR); this is why the mesh is refined in these areas until convergence is achieved.

To reach convergence, the maximum temperature result is analysed using progressively a finer manual mesh size. By doing so, the convergence test will determine if the mesh density is sufficient. If the solution does not converge towards a stable value, it means that the solution is mesh dependent and a finer mesh is required. [66]
The results of the mesh convergence are shown in Table 3.4:

Mesh size	Total number of elements	Temperature
Finer Extremely Coarse Normal	490862	127.8275
Extra fine Extra Coarse Fine	486951	127.827
Extremely fine Coarse Finer	562359	127.827

Table 3.4: Convergence of the maximum temperature in the thermal model

In addition to the convergence test, a quality test is also done by COMSOL. The documentation of COMSOL states that the quality should not go below 0.1 [66]. The quality of the mesh should be very high for the important layers. This is the case as is shown in the mesh quality in Figure 3.4:
The following mesh sizes were used to limit the minimum element quality:

- Extremely fine in the active region and bottom DBR
- Finer in the top DBR
- Coarse in the n-GaN layer and substrate

This allows to keep a high accuracy and keep the number of elements low.

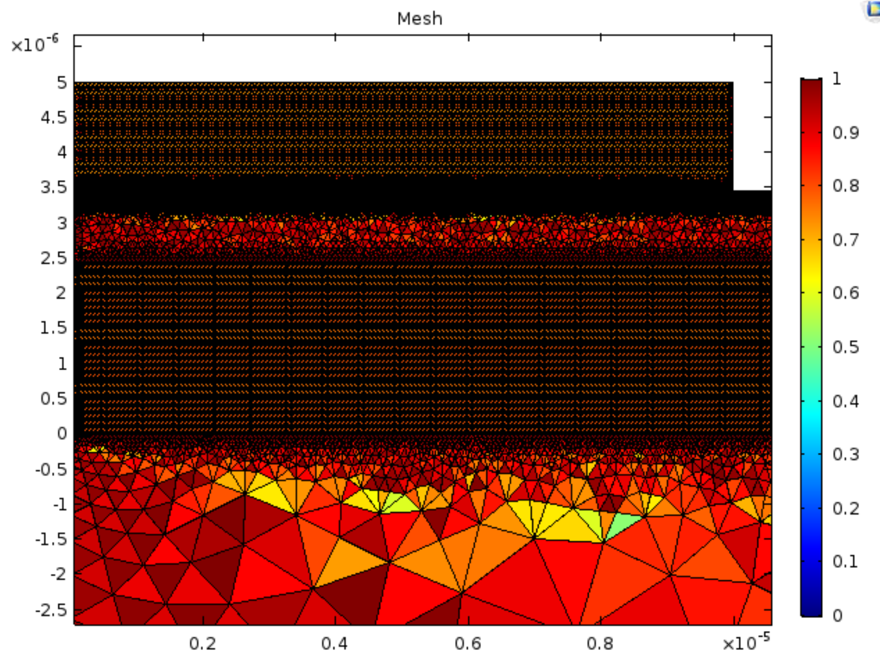

Figure 3.4: Quality of the mesh around the active region

3.8 Simulation results and flux analysis

The results of the simulation allow to compute different values like the temperature in device (1D, 2D or 3D), isothermal contours and also the heat flow that is represented with the arrow surface.

The interesting values to analyse are:

1. Temperature along the optical axis
2. Maximum temperature reached in the active region
3. Isothermal contour
4. Thermal flow

The first item allows to better map the temperature in each layer and to understand the heat flow that takes place in each material. A typical graph is shown in Figure 3.5, where each layer has been colored to better understand the figure.

The maximum temperature in the device will be used to compare the impact of each parameter. It will also be used to compute the thermal impedance $R_{th} = \frac{\Delta T}{P_{diss}}$

where $\Delta T = T_{max} - 20$ °C.

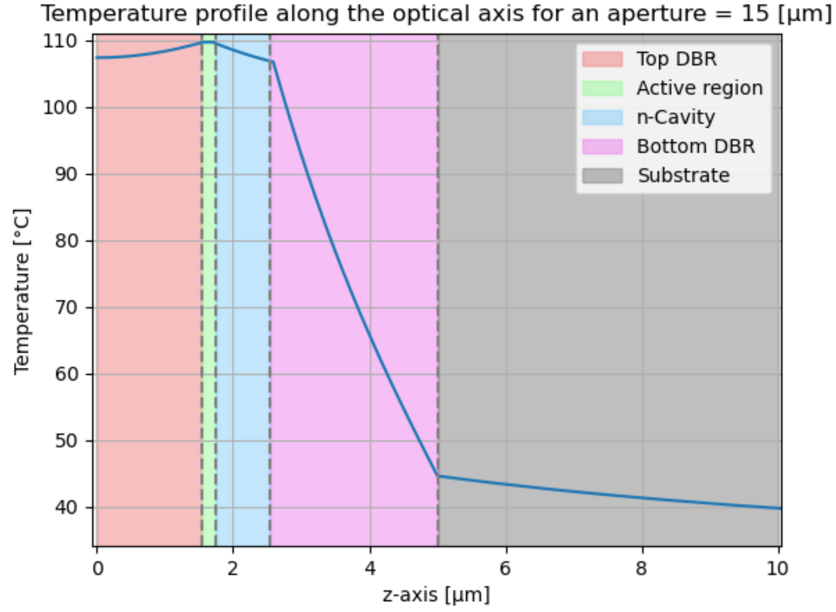

Figure 3.5: Temperature along the optical axis

The last two interesting values allow to better understand the heat flow. It is important to understand how the heat is flowing to estimate the impact of each parameter. This understanding will then be used to design an optimized device.

To analyse the flux, it is useful to plot the isothermal curves of the device at different times to see the evolution of the temperature, this is done in Figure 3.6 and Figure 3.7.

Another important result is the thermal flow that is computed by COMSOL. The results are presented in Figure 3.8. The length of the arrows shows the scale of the heat flow.

All of the figures have been shown for two different sizes of bottom DBR, $w_1 = 35[\mu m]$ and $w_2 = 200[\mu m]$, since the bottom DBR has a low vertical thermal conductivity (8.91 W/mK), it has a huge impact on the heat dissipation. As can be seen in Figure 3.8, the main difference between the two plots is that the heat flow is getting around the confined bottom DBR in Figure 3.8a. This is not the case anymore when the DBR is very large, the heat is mainly spreading

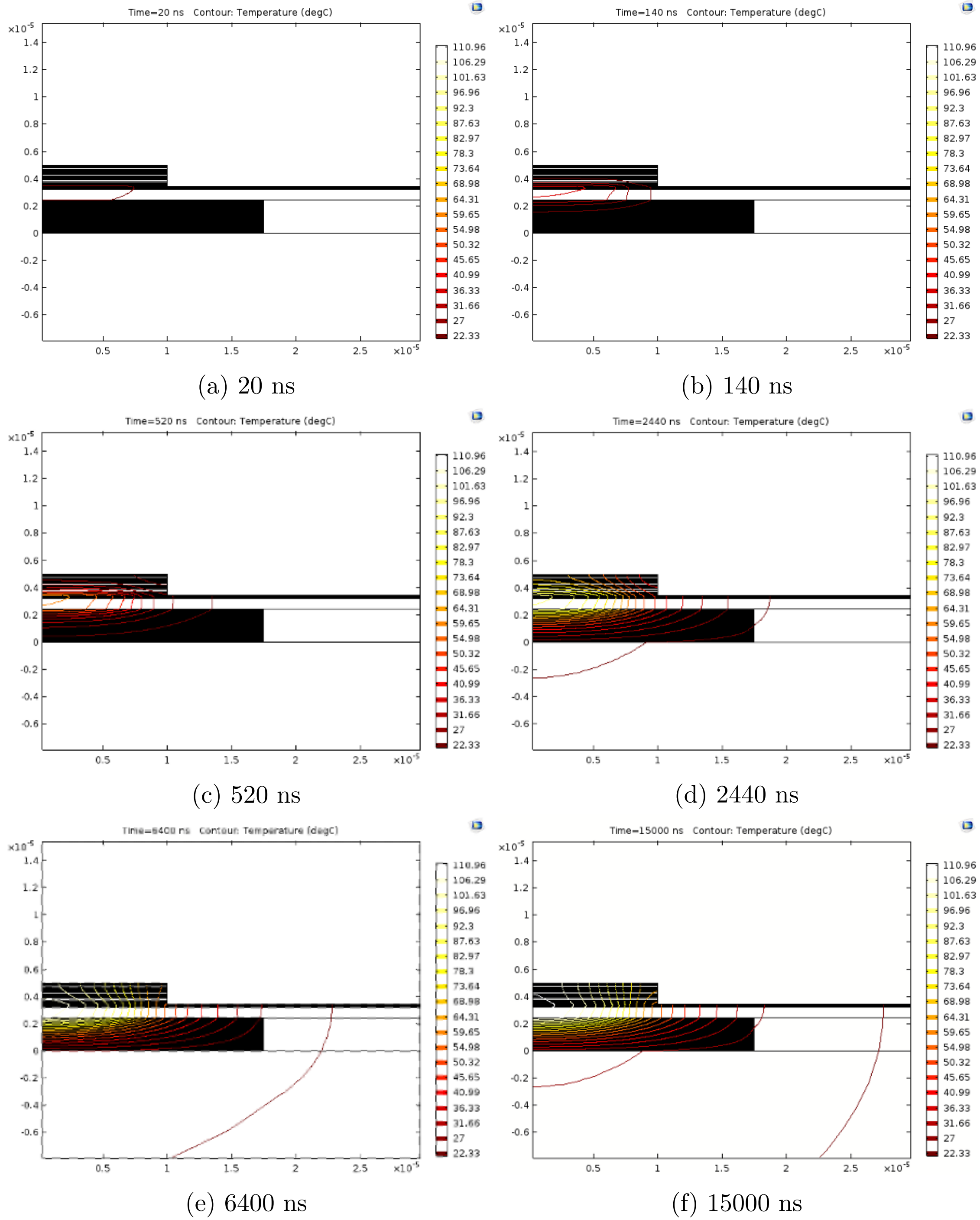

(a) 20 ns (b) 140 ns

(c) 520 ns (d) 2440 ns

(e) 6400 ns (f) 15000 ns

Figure 3.6: Isothermal curves at different times for a DBR width of 35 [μm]

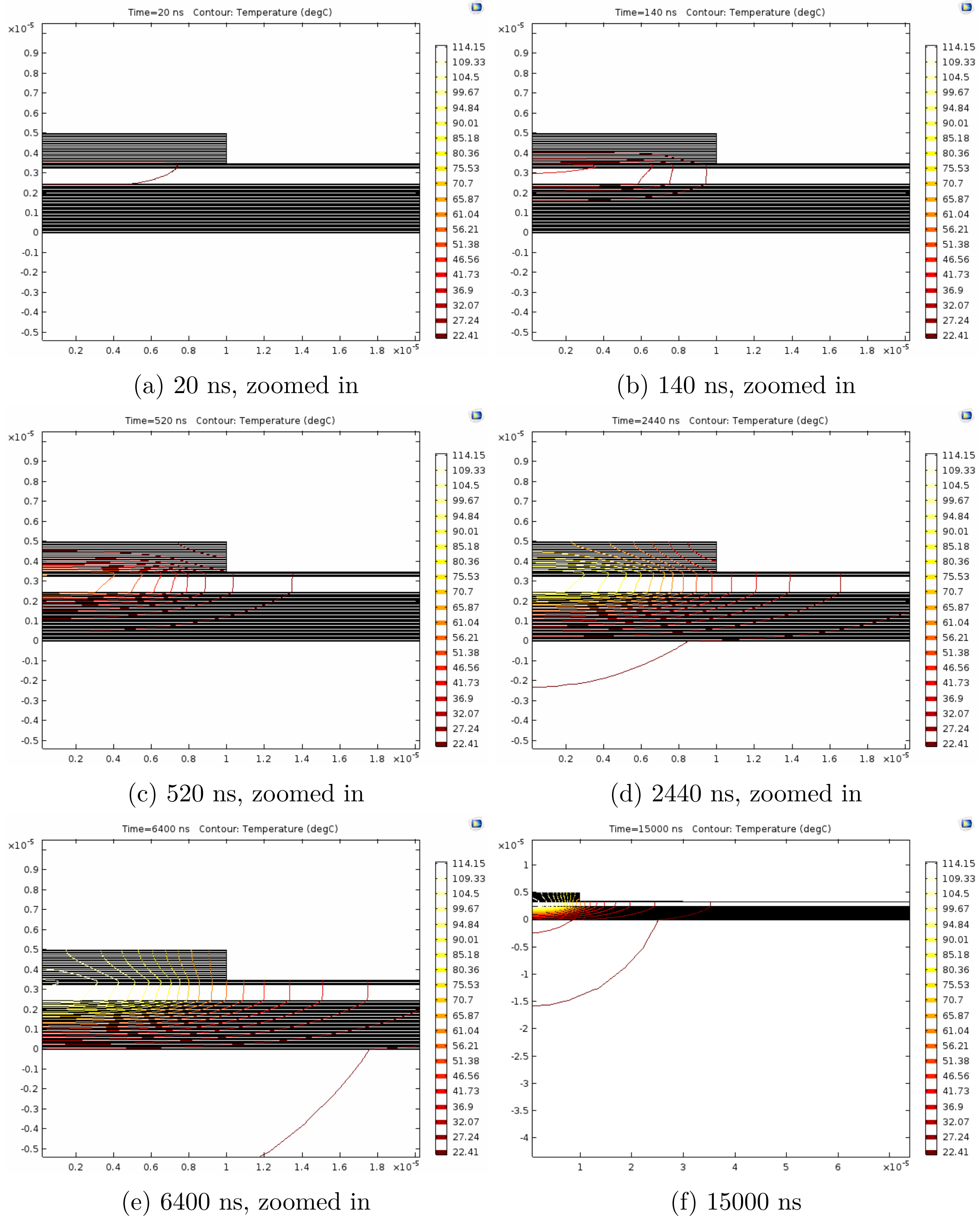

(a) 20 ns, zoomed in

(b) 140 ns, zoomed in

(c) 520 ns, zoomed in

(d) 2440 ns, zoomed in

(e) 6400 ns, zoomed in

(f) 15000 ns

Figure 3.7: Isothermal curves at different times for a DBR width of 150 [μm]

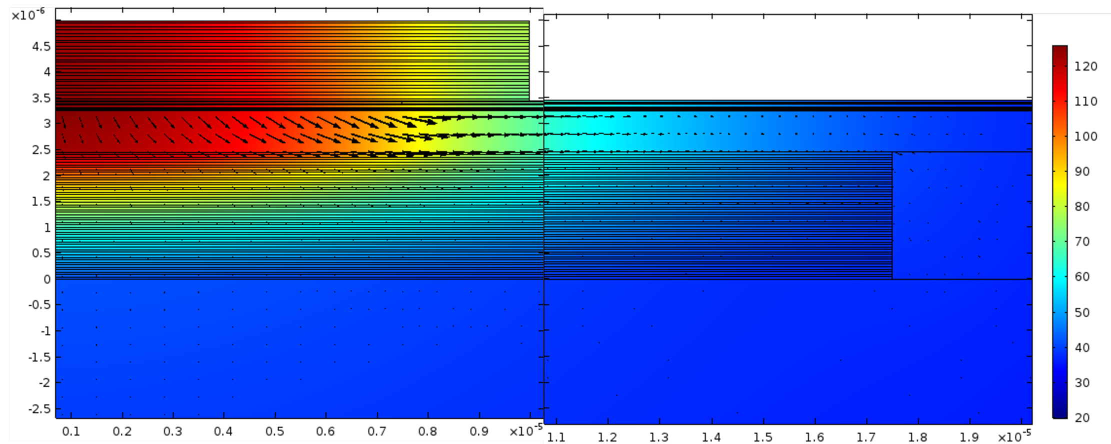

(a) Width DBR = 35 [μm]

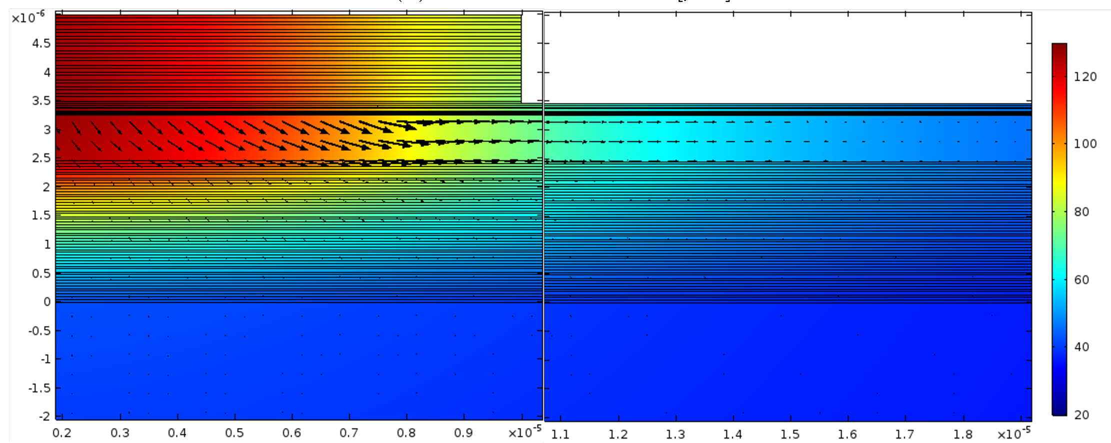

(b) Width DBR = 200 [μm]

Figure 3.8: Thermal flow in the device (zoomed around the active region)

laterally in the cavity Figure 3.8b. This is less visible on the isothermal plots but the impact of the bottom DBR is shown by the fact that the isothermal curve of 22.33 °C in Figure 3.6e is wider than the isothermal curve of 22.41 °C in Figure 3.7e.

As can be seen on the isothermal curves and on the heat flow, the heat is propagating in two ways:

- Spherically around the aperture in the cavity, DBR and substrate
- Laterally further away in the cavity

The heat flow in the cavity is shown in a simple way in Figure 3.9. This will be useful when the impact of the cavity length will be analysed in subsection 4.1.6.

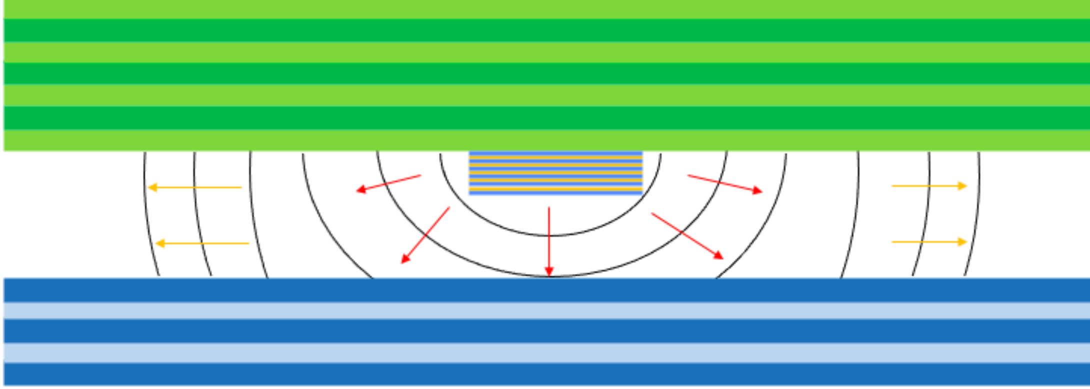

Figure 3.9: Simple representation of the heat flow in the cavity

3.9 Validation with already working VCSELs

It is not possible to validate directly the thermal simulation with an experimental result since the thermal resistance of the NP VCSEL has never been measured. In the section 3.2, where the UCSB structure was simulated, the thermal resistance is:

$$R_{th} = \frac{267°C - 20°C}{0.1W} = 2470°C/W \tag{3.11}$$

This is in good agreement with what has been reported experimentally by Forman [10]: a thermal resistance of 2750 °C/W.

Another solution to validate the simulations is to compare the obtained results with an AlInN DBR VCSEL since AlInN has also a very low thermal conductivity: 4.89 W/mK[82, 83], comparable to a porous GaN layer.
The AlInN/GaN DBR has:

- κ_r = 64.98 K/mW
- κ_v = 9.06 K/mW

These values are slightly better than the porous DBR (κ_r = 61.19 K/mW and κ_v = 8.91 K/mW), otherwise the structure is nearly similar to the NP GaN, as is described in [64].

The obtained thermal resistance of the porous DBR is:

$$R_{th} = \frac{109.73°C - 20°C}{0.088357W} = 1015°C/W \tag{3.12}$$

This is close to the experimental value computed by Meijo: 1100 °C/W [64]. However the value of 1100 °C/W is the thermal resistance of a flipped device, this can explain the difference between the values.

Chapter 4

Simulations and optimization

Contents

4.1 Influence of parameters **50**
4.1.1 From pulsed to CW 51
4.1.2 Bottom DBR width 53
4.1.3 Number of pairs of the bottom DBR 55
4.1.4 Porosity 56
4.1.5 Aperture 59
4.1.6 Cavity length 63
4.1.7 Substrate thickness 65
4.1.8 Mechanical stress analysis 67
4.2 Perspectives **69**
4.2.1 Optimization of the thermal management 69
4.2.2 Flip-chip 73

Overview

Now that the model is validated, the influence of parameters of the VCSEL is analysed to decrease the temperature inside the device. Once the thermal management is better understood, an optimized structure will be proposed.

4.1 Influence of parameters

All the parameters that will be analyzed are shown in Figure 4.1

1. Bottom DBR width
2. Number of bottom DBR pairs
3. Porosity of porous layer
4. Aperture width
5. Cavity length
6. Substrate thickness

Figure 4.1: Structure of the device with the parameters that will be analysed

To analyse the influence of each parameter individually and to identify key design parameters which have the largest influence on thermal resistance, the simulations have all been computed with the same parameters:

1. Bottom DBR width = $200[\mu m]$
2. Number of bottom DBR pairs = 25
3. Porosity = 40%
4. Aperture = 15 $[\mu m]$
5. Cavity length = 6λ
6. Substrate thickness = 500 $[\mu m]$

4.1.1 From pulsed to CW

A strong thermally dependent behaviour is observable in VCSELs due to the severe heating caused by the poor heat dissipation and high thermal impedance of the DBRs. [58] A huge difference between pulsed and CW operation is thus expected. First the pulsed operation will be analysed.

Usually the fabricated VCSEL devices are tested under pulsed current conditions to avoid the operation heating. This pulsed operation can be simulated in COMSOL by using a periodic heat load and using the Events interface. A pulse width of 200ns is simulated with a duty cycle of 0.4% as is done in [47]. The input power is 0.4[W], since the turn-on voltage and lasing threshold current density are 5.4 V and 42 $\frac{kA}{cm^2}$ respectively.

In Figure 4.2, the evolution of the temperature in the active region is shown. It is interesting to see that even a very short pulse of 200 ns causes a temperature rise of 110 °C (130 °C - 20 °C) . It is also clear in this figure that due to the very small duty cycle, there is no self-heating.

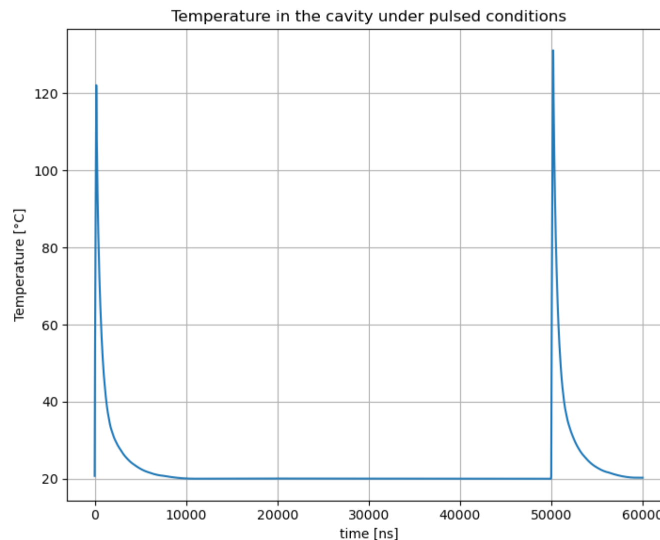

Figure 4.2: Evolution of the temperature in the active region with time under pulsed conditions

An interesting parameter to analyse is the time that is needed to reach the steady-state temperature. This is plotted in Figure 4.3.

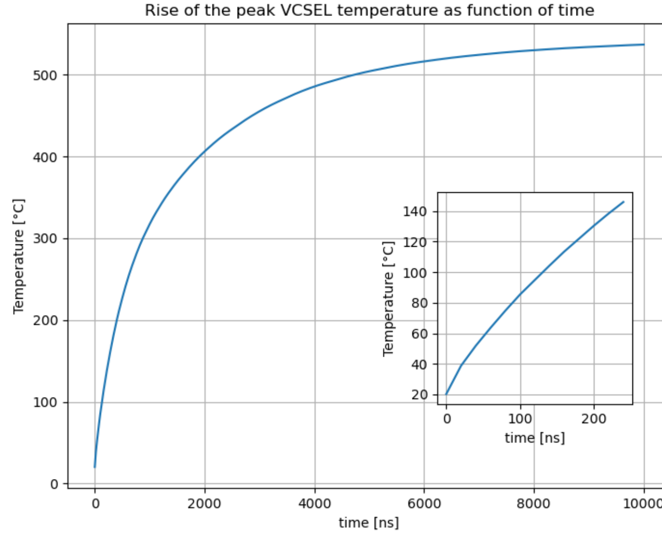

Figure 4.3: Rise of the peak VCSEL temperature as function of the time, with a zoom on the first 200 ns.

This shows that the transient temperature rise during the pulsed laser operation is not negligible. And as shown in the inset, a short pulse of 200 ns, leads to a temperature of 130 °C, which corresponds to an increase of 110 °C, as mentioned above. More than half of the steady-state temperature rise is reached after only 687 ns.

From now on, the threshold current density that will be used is $j_{th} = 10\ [\frac{kA}{cm^2}]$ and the turn-on voltage is 5 [V]. This corresponds to the threshold current density value that is expected for the next batch of blue NP VCSEL devices. This allows to have a better estimation of the final device.

The impact of each parameter is computed with the 2D-axisymetric steady-state simulation. The temperature that is computed with the steady-state simulation corresponds to the temperature that is reached after a few milliseconds. By working with a steady-state simulation instead of a time-dependent simulation, the simulation time is greatly reduced.

4.1.2 Bottom DBR width

All the NP VCSELs that have been created before by Yale University, have always had a bottom DBR that reached along the whole width of the device. But it could be interesting to analyse the impact of a confined DBR. The GaN that surrounds the DBR could act like a conducting ring for the heat flow, since GaN has a high thermal conductivity.

The influence of the width of the bottom DBR has been simulated and the evolution of the highest temperature in the device is presented in Figure 4.7. The aperture width and the width of the device are also shown to facilitate the comparison with the dimensions and other parameters of the device.

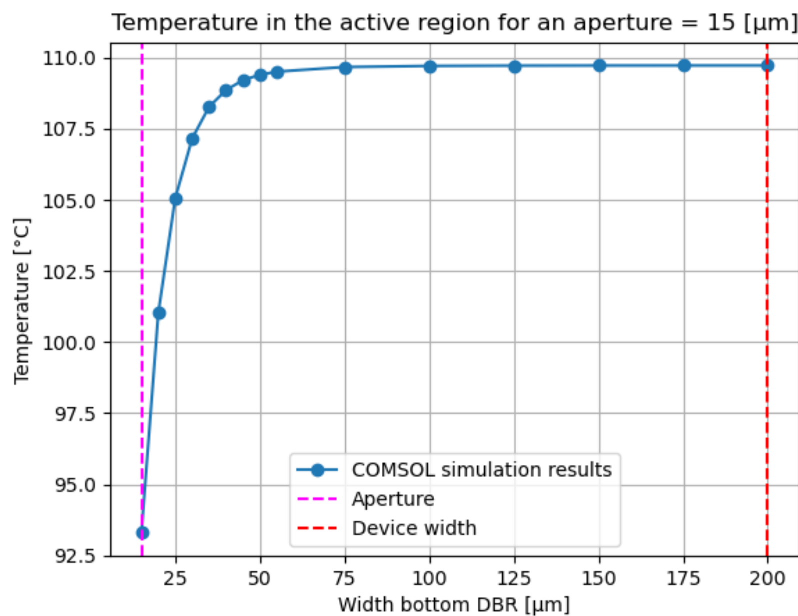

Figure 4.4: Evolution of the temperature in the active region depending on width of the bottom DBR

To analyse the impact of this parameter, two cases need to be differentiated:

1. When the width of the DBR is still small enough to allow the heat flux to get around the DBR and to flow through the GaN that surrounds the DBR.
2. The heat flux mainly passes through the bottom DBR

In the first case, this is $w_{DBR} < 50\mu m$, the slope of the temperature in the bottom DBR (grey zone), is not the same for each DBR width, as can be seen in Figure 4.5. This can only be explained by the fact that the heat flux is getting around the bottom DBR, since the properties of the bottom DBR stay the same at each iteration.

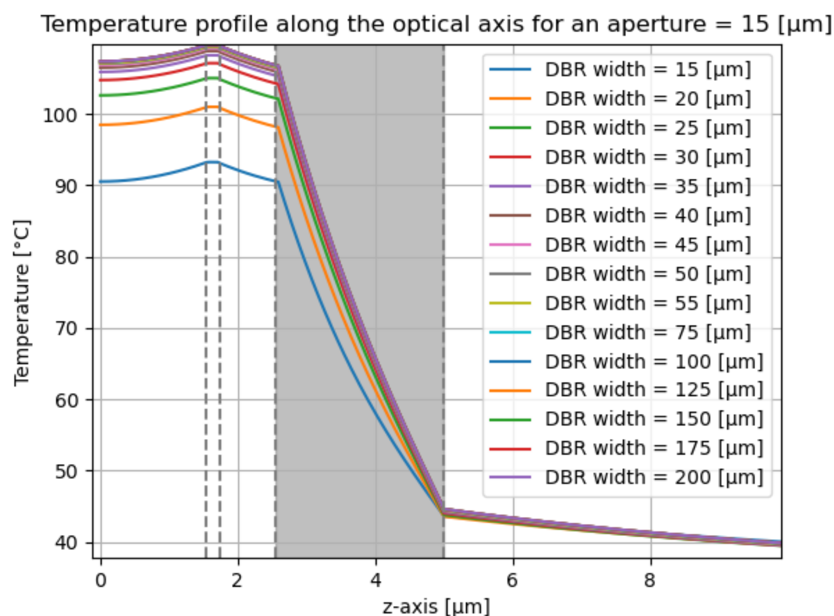

Figure 4.5: Temperature in the device along the optical axis for different DBR widths, the grey area corresponds to the bottom DBR

When the heat flow is getting through the surrounding GaN, the thermal resistivity of the bottom DBR layer is reduced since GaN has a high thermal conductivity. The temperature in the device is thus reduced.

In the second case, as already said, the heat flow is mainly going through the bottom DBR. This is why the temperature is not evolving anymore once the bottom DBR reached a width of 50 [μm]. All the curves above 50 μm are superposed.
When the aperture is smaller, the saturation of the temperature happens at smaller DBR widths. This is logic since the heat dissipates less in the lateral way for devices with smaller apertures. The same plot as Figure 4.4 is shown for an aperture of 6 and 8 μm. As can be seen in Figure 4.6.
From Figure 4.4, it seems a good idea to decrease the bottom DBR width to reduce the temperature in the device. However, by decreasing the diameter of the bottom DBR, the alignment tolerance during the VCSEL fabrication would be lowered

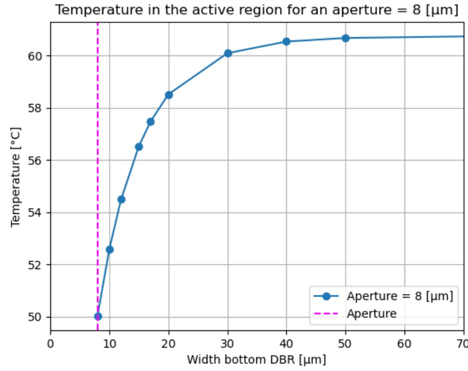

(a) Aperture = 8 [μm]

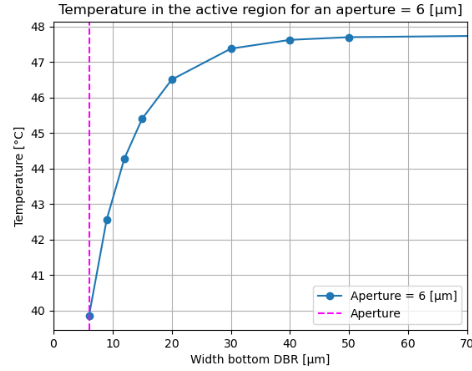

(b) Aperture = 6 [μm]

Figure 4.6: Evolution of the temperature along the optical axis for different DBR widths

[50]. This limitation will be taken into account when optimizing the device in subsection 4.2.1. The bottom DBR minimum width is limited to the aperture otherwise the VCSEL would not be able to lase.

4.1.3 Number of pairs of the bottom DBR

The influence of the number of pairs of the bottom DBR has been simulated and the evolution of the highest temperature in the device is presented in Figure 4.7.

The curve has been interpolated with a second order equation in python.

$$f(N) = -0.0277N^2 + 2.0703N + 73.9771 \tag{4.1}$$

Even if the relation is quadratic, the relation can be approximated by a linear relation since the coefficient of the quadratic term is two orders smaller than the coefficient of the linear term.

By considering the impact of this parameter as linear, it is easy to understand that by increasing the number of pairs of bottom DBR, the thermal path to the substrate is linearly raised and the temperature will thus linearly increase too.

The same simulations have been performed with a bottom DBR width of 35 [μm]. The curve has been interpolated by the following equation:

$$f(N) = -0.0252N^2 + 2.0691N + 73.9258 \tag{4.2}$$

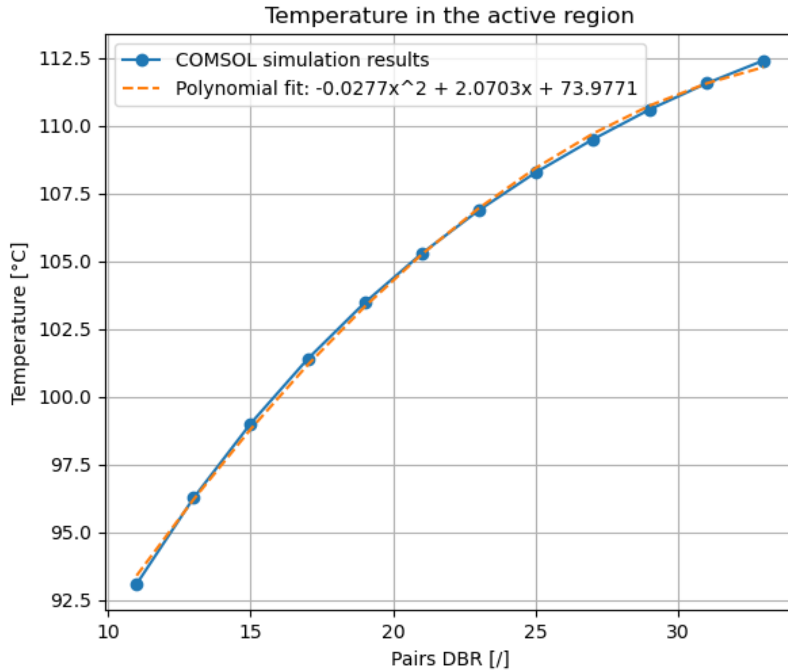

Figure 4.7: Evolution of the temperature in the active region depending on the number of pairs of the bottom DBR

Compared to Equation 4.1, both quadratic and linear term have decreased a bit. This confirms the flux analysis, explaining that the bottom DBR has less impact when the diameter is smaller since a part of the heat is getting around the DBR.

4.1.4 Porosity

The thermal conductivity and refractive index of porous GaN, based on Equation 3.9, are shown in Figure 4.8. It can be seen that the thermal conductivity of the porous layer is decreasing when the porosity is increasing. This is normal since air is nearly a thermal insulator (0.0256 [W/mK] [84]) while the thermal conductivity of GaN is assumed to be 130 [W/mK]. The refractive index of the nanoporous layer decreases also when the porosity increases. This is due to the refractive index of air that equals 1 while the index of GaN is 2.5063.

By increasing the porosity, the thickness of the NP layer will decrease since the thickness of a DBR layer is equal to a quarter of the wavelength:

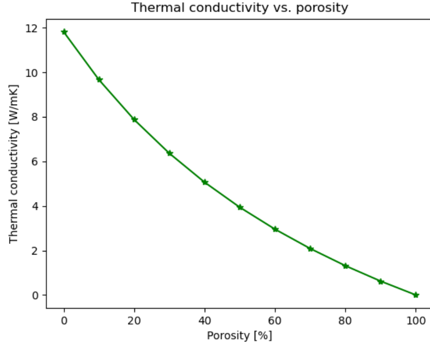

(a) Thermal conductivity of NP layer

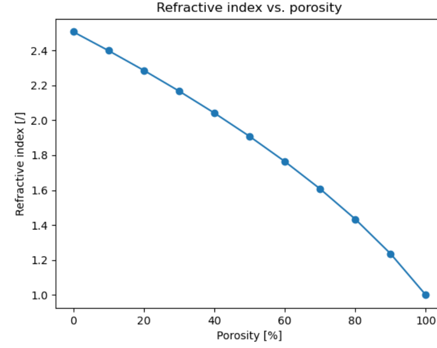

(b) Refractive index of NP layer

Figure 4.8: Thermal and optical values of NP layers versus the porosity of the layers

$$t_{\text{NP layer}} = \frac{\lambda}{4 \times n_{NP}} \tag{4.3}$$

When the porosity of the mirror is changed, it will also impact the reflectance spectrum of the DBR. The peak of the reflectance evolves according to the following equation [28]:

$$R = \Big[\frac{1 - (\frac{n_L}{n_H})^{2m}}{1 + (\frac{n_L}{n_H})^{2m}}\Big]^2 \tag{4.4}$$

where m is the number of pairs in the DBR, n_L is the lower refractive index and n_H is the higher refractive index of the two alternating layers in the mirror. The peak reflectance is improved when the porosity increases, as shown in Figure 4.9b. Another important value is the width of the high-reflectance band of the mirror, $\Delta\lambda_{max}$, this stopband width is expressed as [28]:

$$\Delta\lambda_{max} = \frac{4\lambda}{\pi} asin(\frac{\Delta n}{n_H + n_L}) \tag{4.5}$$

This value is sensitive to $\Delta n = n_H - n_L$. A high porosity is thus required for a wide stopband width (Equation 4.5) and a high peak reflectance (Equation 4.4).

In reality, when a finite number of pairs is used, the "usable" reflectance bandwidth, $\Delta\lambda_{usable}$, is much smaller than $\Delta\lambda_{max}$. This usable stopband width is computed as follows for high performance VCSELs : R > 0.995. Another value of interest is the normalized ratio $\frac{\Delta\lambda_{usable}}{\lambda}$, this value is more pertinent for the manufacturability of the VCSEL. It needs to stay above 0.02 to ensure a certain margin against

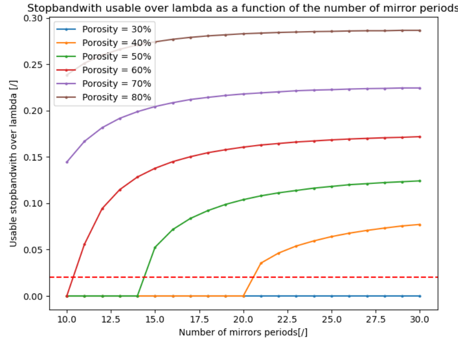

(a) Usable stopbandwidth of the DBR depending on the porosity of the NP layers

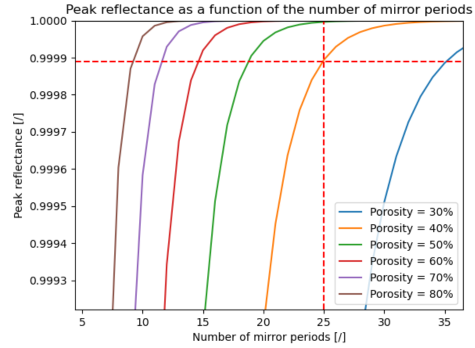

(b) Peak reflectance of the DBR depending on the porosity of the NP layers

Figure 4.9: Impact of the porosity on the DBR performances

non-uniformities and variations during the fabrication processes.[28] This is shown in Figure 4.9a.

Now that the impact of the porosity on the NP layers has been explained, the impact of the porosity on the temperature in the VCSEL is analysed.
To determine the numbers of layers of the bottom DBR depending on the porosity, the following was done:

- First determine the minimum number of layers that is required for the manufacturability of the VCSEL, based on Figure 4.9a
- Next the same peak reflectance was chosen as what is done in [47]: 25 pairs at 40%.

The result is shown in Table 4.1

30%	40%	50%	60%	70%	80%
/	25	19	15	12	10

Table 4.1: Number of pairs in the NP DBR depending on the porosity

The impact of the porosity is shown in Figure 4.10 for a DBR width of 35 and 200 [μm] respectively.
The same can be concluded as for the number of bottom DBR pairs where the impact of the porosity is more linear if the width of the DBR is small. If the DBR is larger, the impact of the porosity is more quadratic as explained by the flux.

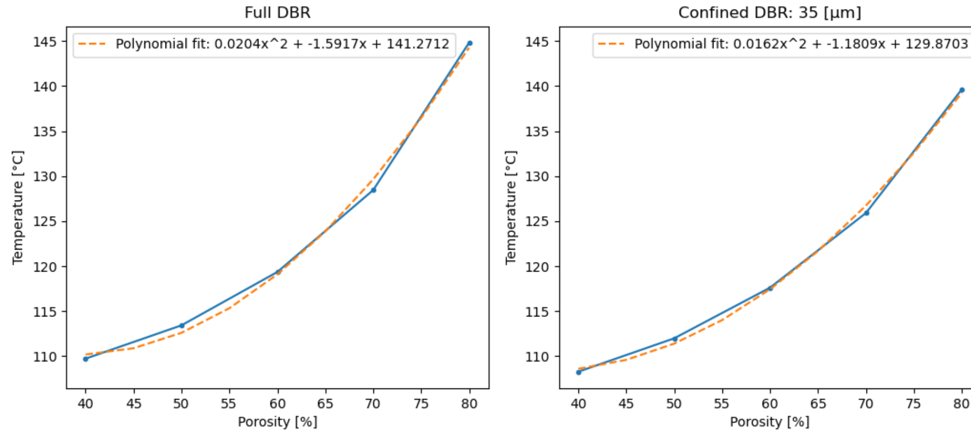

Figure 4.10: Evolution of the temperature in the active region depending on the porosity for two different DBR widths

From this graph, it can be concluded that the lowest porosity is better to decrease the temperature in the device. On the other side, it cannot be reduced below 40% otherwise the mirror wouldn't be stable enough, as explained before. Depending on the width of the DBR, the impact of the porosity is more pronounced. It is thus better to choose for a lower porosity when the DBR is large. The porosity can be increased to improve the mechanical stability of the mirror for a confined DBR.

4.1.5 Aperture

The impact of the aperture is more complex to understand than the other parameters since not only the geometric aspect needs to be taken into account but also the injected power, since the current density is kept constant and not the dissipated power.

The impact of the aperture on the temperature is shown in Figure 4.11.
The temperature is linearly increasing with the aperture. To better understand this trend, the evolution of the dissipated power with the aperture is shown, as well as the evolution of the temperature with the injected power, at a constant aperture of 15[μm].
As can be seen in Figure 4.12a, the dissipated power is quadratically increasing with the aperture. This can easily be explained with the equation used in Table 3.1 where the dissipated power is the multiplication of the current by the voltage and the current equals the current threshold density times the area of the active region:

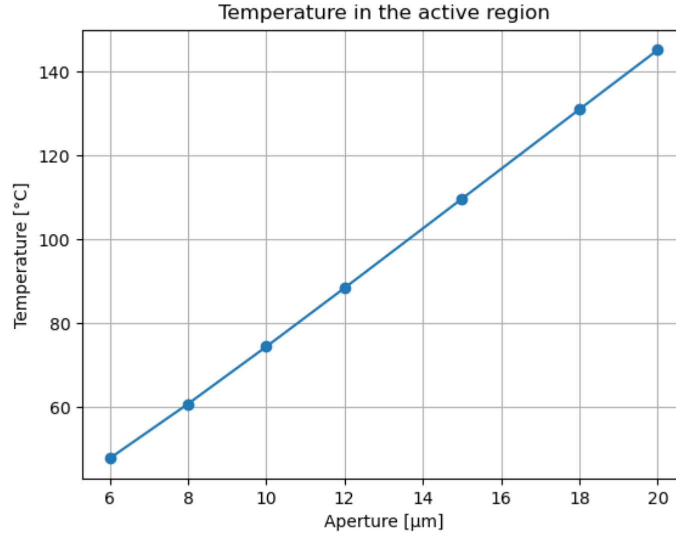

Figure 4.11: Evolution of the temperature in the active region as a function of the aperture width

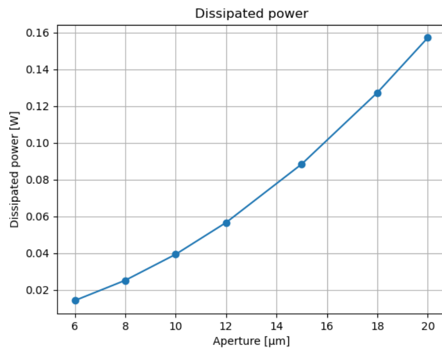

(a) Impact of the aperture on the dissipated power

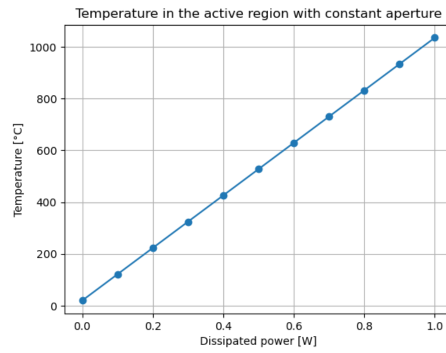

(b) Influence of the dissipated power on the temperature

Figure 4.12: Influence of the aperture and the dissipated on the temperature

$$I = j_{th} \times \pi(\frac{aperture}{2})^2 \tag{4.6}$$

$$V_{active} = (t_{QW} \times N_{QW}) \times \pi(\frac{aperture}{2})^2 \tag{4.7}$$

$$P_{diss} = V \times I \tag{4.8}$$

$$P_{dens} = \frac{P_{diss}}{V_{active}} \tag{4.9}$$

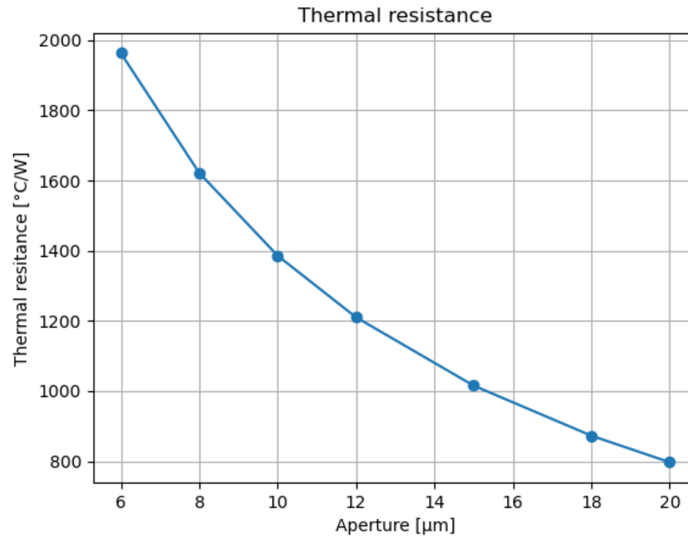

Figure 4.13: Evolution of the thermal impedance with the aperture

Where the power density is simply obtained by dividing the dissipated power by the volume of the active region.

Another interesting value to analyse is the increase of the temperature with the injected power. In this simulation, the geometrical part is not taken into account since the aperture is not changing. As can be predicted, the temperature is proportional to the injected power, as shown in Figure 4.12b.

The linear relation between the temperature and the aperture can now be explained in an easy way:

- By keeping the power density constant, a wider active region increases the total dissipated power in the active region, increasing the temperature in a quadratic way.
- The heat dissipation is enhanced by increasing the surface area of the active region. By increasing the aperture, the heat flow is improved and will reduce the temperature in the device linearly.

Taking both points into account, the linear increase of temperature can be explained by the increase of the dissipated power and the heat flow improvement. The last figure that is interesting to analyse is the evolution of thermal impedance with the aperture. This is shown in Figure 4.13

This evolution can also be seen in [8, 49] but it is mainly explained by the larger surface area. It is only said that a trade-off condition is required. This is not really accurate since the lowest temperature will always be reached with the lowest aperture since the power density is assumed to be constant.

The thermal impedance is thus lower for wider apertures due to enhanced heat dissipation and also because the thermal impedance can be written as:

$$R_{th} = \frac{\Delta T}{\Delta P} = \frac{\frac{\Delta T}{\Delta r}}{\frac{\Delta P}{\Delta r}} = \frac{r}{r^2} = \frac{1}{r} \tag{4.10}$$

Where r stands for the radius of the aperture. It can thus be concluded that a wider active region is more efficient for heat dissipation (low thermal resistance) but the temperature in the active region will be warmer due to higher injected power.

Following this conclusion, a smaller aperture is thus needed to reach low temperature but there exists a limitation to the aperture. The threshold current density increases when the aperture is smaller than 4[μm] as can be seen in [3, 4], due to the increased diffraction and scattering losses as well as a decreased transverse confinement factor Γ_{active}. [22, 50]

The increase of diffraction loss per round trip is shown in Figure 4.14. It derives from decoupling of the beam profile [85]. It can be seen that by decreasing the aperture, the losses are reduced, while the cavity length needs to be reduced to limit the losses per roundtrip.

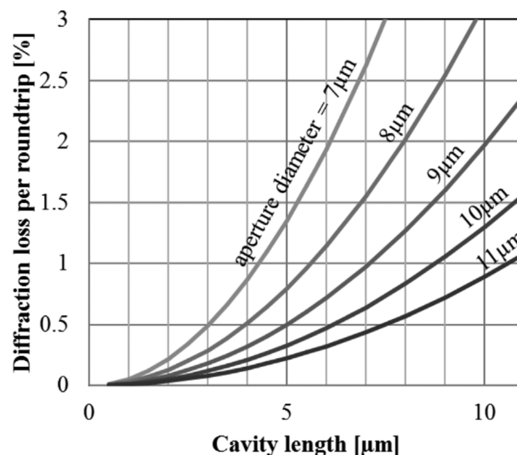

Figure 4.14: Diffraction loss per roundtrip [85]

4.1.6 Cavity length

When the thickness of the cavity is changed, it is usually the thickness of the n-GaN layer that is changed. It would be complicated to change the thickness of some layers in the p-side of the cavity since is very complex as structure. The same has been done in COMSOL: by changing the cavity thickness, the n-GaN layer thickness is modified.

The impact of the cavity length = mλ on the temperature is shown in Figure 4.15.

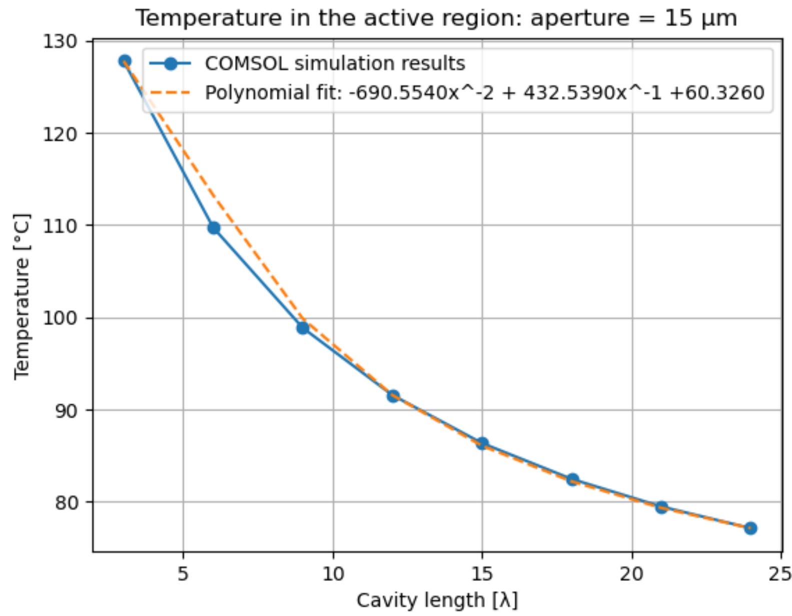

Figure 4.15: Evolution of the temperature in the active region depending on the cavity length

From this plot, it is clear that the evolution follows the fitting equation:

$$f(N) = \frac{-690.554}{m^2} + \frac{432.539}{m} + 60.326 \tag{4.11}$$

So we can conclude that the impact of the cavity is quadratic and linear. This can be explained by the thermal flux. As shown in the simple representation of the flux in the cavity in Figure 3.9, the flow has two main components:

- A linear component that stands for the lateral term.
- A spherical component that induces the quadratic term.

From Figure 4.15, it is clear that by increasing the thickness of the cavity, the temperature will be reduced. A larger cavity volume increases the lateral thermal heat dissipation and avoids that the heat stays concentrated around the active region. The high thermal conductivity of GaN enhances the spherical and lateral heat transfer in the device.

As can be seen in Figure 4.16, the impact of the cavity is smaller when the aperture is decreased to 6 μm. The temperature drop induced by the cavity is only ≈ 20 °C, while the drop ≈ 50 °C in Figure 4.15.

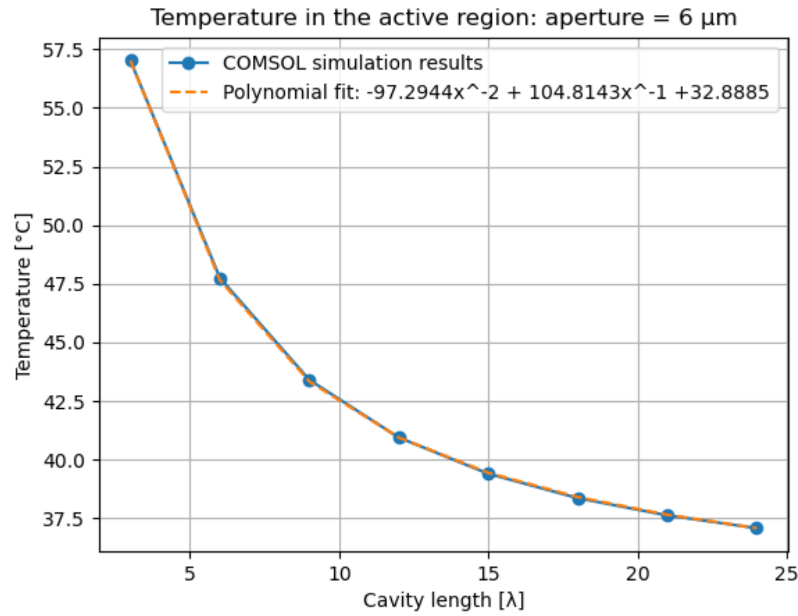

Figure 4.16: Evolution of the temperature in the active region depending on cavity length for an aperture of 6 [μm]

This smaller impact is also visible in the coefficients that fit the curve:

$$f(N) = \frac{-97.294}{m^2} + \frac{104.814}{m} + 32.888 \tag{4.12}$$

The quadratic as well as linear term are both reduced, since the aperture is smaller, which reduces the heat spreading.

However, increasing the thickness of n-GaN layer can be detrimental for UV applications as GaN becomes highly absorbing at these wavelengths. [8] Furthermore a short cavity can be used for a single longitudinal mode emission due to the large

mode spacing. [50] Other drawbacks of longer cavities are the increased absorption loss and diffraction loss (cf. Figure 4.14) and the reduction of the longitudinal confinement and the spontaneous emission factor.[2]

4.1.7 Substrate thickness

The impact of the substrate thickness is shown in Figure 4.17.

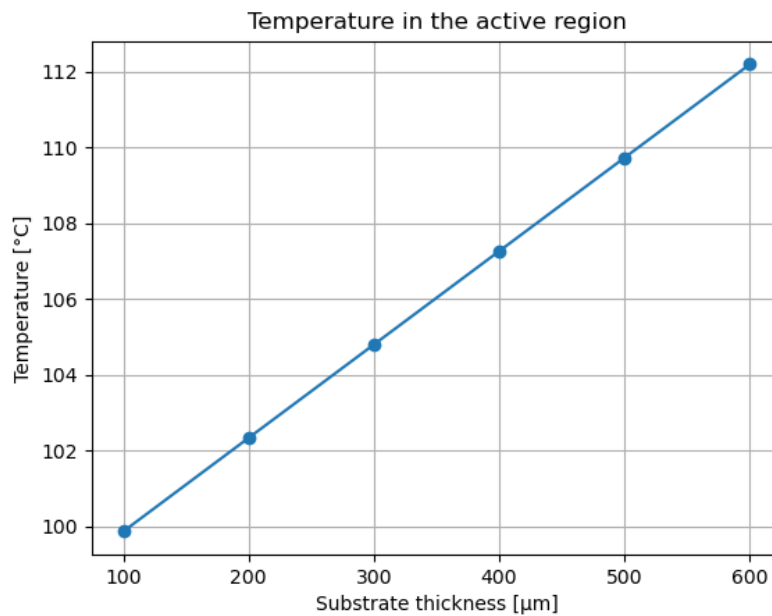

Figure 4.17: Evolution of the temperature in the active region depending on the substrate thickness

It is interesting to analyse the impact of the substrate thickness. This can be done easily with the heat transfer rate, since there is no heat source in the substrate.

In the absence of any volume heat sources, the conservation equation of energy in a uniform solid in steady state is written in local form as:

$$\nabla \cdot q = 0 \tag{4.13}$$

where q is the heat flux density vector $[\frac{W}{m^2}]$, that can be related to the temperature with Fourier's law:

$$q = -k\nabla T \tag{4.14}$$

When the heat is flowing through a constant area A, the heat flux density q can be related to the heat transfer rate $\frac{\mathrm{d}Q}{\mathrm{d}t}$ through the following relation:

$$\frac{\mathrm{d}Q}{\mathrm{d}t} = A \cdot q \tag{4.15}$$

The expression of the temperature field along the substrate is then given by a linear relation: T(z) = Az + B, by assuming that all the heat transfer in the substrate is vertical. This is verified by looking at Figure 4.18, where the slope of the temperature in the substrate stays the same at each iteration for a different substrate thickness.

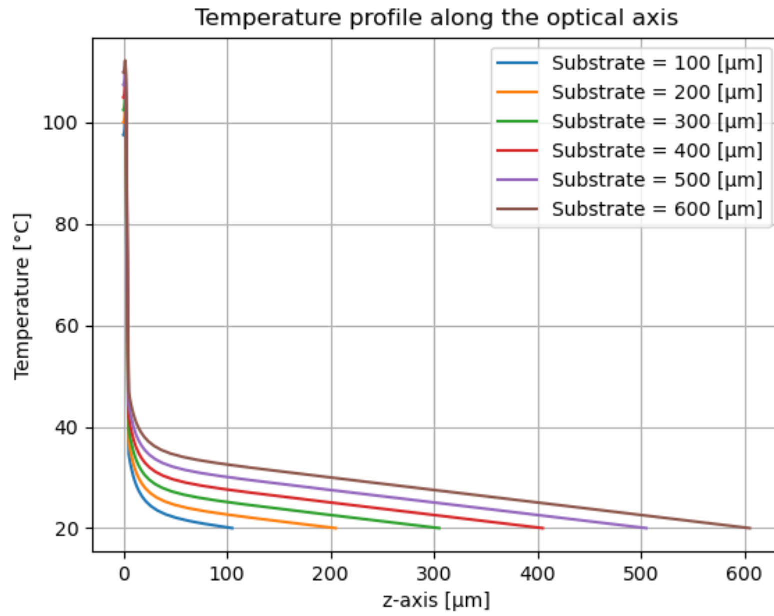

Figure 4.18: Temperature in the device along the optical axis for different substrate thicknesses

Now that the expression of the temperature is known, the heat transfer rate can be expressed by:

$$\frac{\mathrm{d}Q}{\mathrm{d}t} = -kA\frac{T_c - T_h}{d} \tag{4.16}$$

where T_h is the temperature at the hot side of the substrate and T_c is the temperature at the cold side of the substrate, in this case 20 °C. A is the surface perpendicular to the heat flux and d is the thickness of the substrate layer.

The temperature at the interface between the substrate and the bottom DBR can thus be expressed as:

$$T_h = T_c + \frac{\mathrm{d}Q}{\mathrm{d}t}\frac{d}{kA} \tag{4.17}$$

Since the heat flux coming from the bottom DBR stays constant when changing the substrate thickness, the temperature T_h will only depend on the thickness of the substrate d. This can be demonstrated by showing that the increase in temperature with the thickness is constant. This confirms the hypotheses made before that gave a linear relation.
As presented in Figure 4.19, the increase in temperature at each iteration is around 2.467 °C for an increase of the thickness of 100 μm. It is clear that the impact of this parameter is not as important as the other parameters.

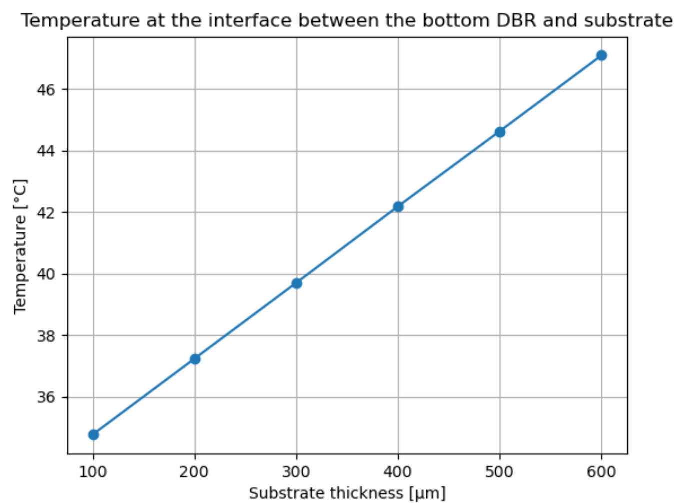

Figure 4.19: Increase of the temperature at the interface of the bottom DBR and substrate, with the substrate thickness

This can also be seen in Figure 4.17, where the temperature increases with the same slope: $\frac{2.467°C}{100\mu m}$.

4.1.8 Mechanical stress analysis

It is interesting to analyse the impact on the mechanical behaviour of the device. To do so, the solid mechanic physics needs to be added to the COMSOL model and the bottom needs to be constraint as a fixed boundary. The necessary multiphysics couplings to add are:

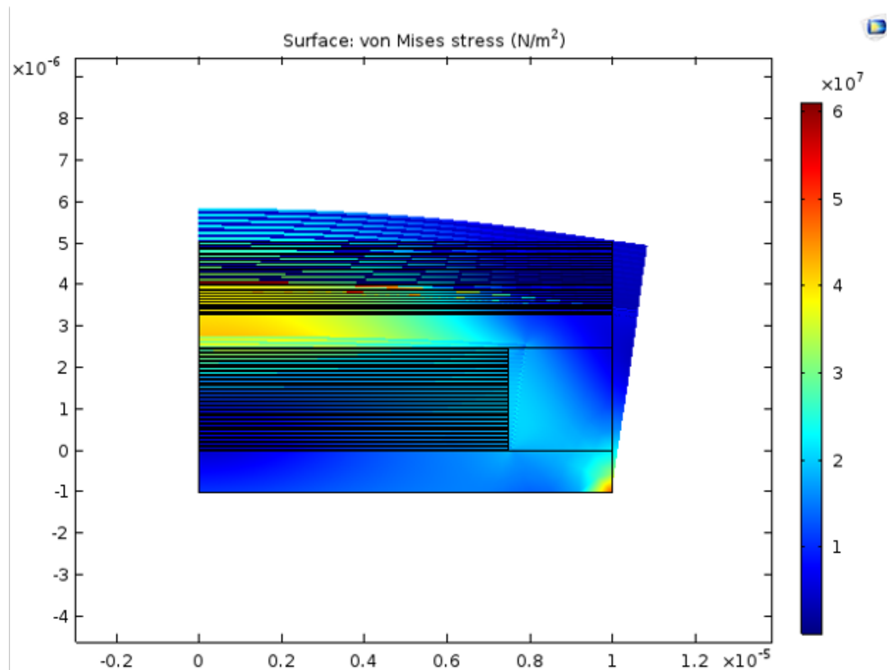

Figure 4.20: Stress and deformation due to heating

- The thermal expansion to model deformation and displacement
- The temperature coupling to pass the temperature from the heat transfer in solid interface to the solid mechanics interface.

The stress is plotted in Figure 4.20, the deformation is also visible in this figure. This deformation has been greatly exaggerated to better see the mechanical impact. The 10 MPa stress is not critical in the device. It is clear that most of the stress is occurring at the edge of the device, but this is not critical for the performance of the device since it is not occurring in the cavity and it doesn't spread widely in the device.

The stress that occurs in the active region is probably an artefact since no constraints are acting on the this region. It is able to freely expand.

4.2 Perspectives

4.2.1 Optimization of the thermal management

Now that the impact of all the parameters has been analysed, the device can be optimized to improve the thermal management. Some algorithms exist like the genetic algorithm. This algorithm was developed by John Holland in 1960s and 1970s. He created a model based on the biological evolution of Charles Darwin's theory of natural selection [86]. Even though this algorithm has many advantages, no optimization algorithm has been used since the impact of each parameter is straightforward.

To better compare the impact of each parameter, the evolution of the cavity temperature with each parameter is shown in Figure 4.21, where the y-axis has the same range to have a global view on the impact of all those parameters.

From Figure 4.21, it is clear that the aperture is the parameter that induces the highest temperature increase (going from a 6[μm] aperture to a 20[μm]: 47.75 to 145.24 °C increase). The next parameter that has a big influence on the temperature in the device is the cavity length; by increasing the cavity length from 6λ to 24 λ, the temperature decreases by 50.7 °C (127.8 - 77.1). The width of the bottom DBR is the next parameter with the highest impact on the temperature. Reducing this width to a value lower than 50 [μm] allows to decrease the temperature by 16 °C (109.7 - 93.3).

As explained in previous subsections, the aperture, cavity length and bottom DBR are all limited by some constraints. The aperture is limited by the threshold current density. Choosing for a 6 [μm] aperture is a compromise between the decreasing temperature and the increasing current density for small apertures, as well as increasing diffraction losses.

The cavity length is the second parameter with the most impact. This is why this parameter is usually chosen to improve the thermal management [8, 9, 64, 10]. However increasing the cavity will induce higher diffraction losses, which is not intended. A cavity of 9 λ is thus chosen as trade-off between the temperature and the losses, as shown in Figure 4.14.

Since the confined DBR has never been created, two solutions will be proposed: one with a full DBR and one with a confined DBR. Confining the DBR is limited by fabrication alignment tolerance. Choosing for a DBR diameter that is too small will increase the risk of misalignment. A diameter of 15 [μm] is thus chosen as

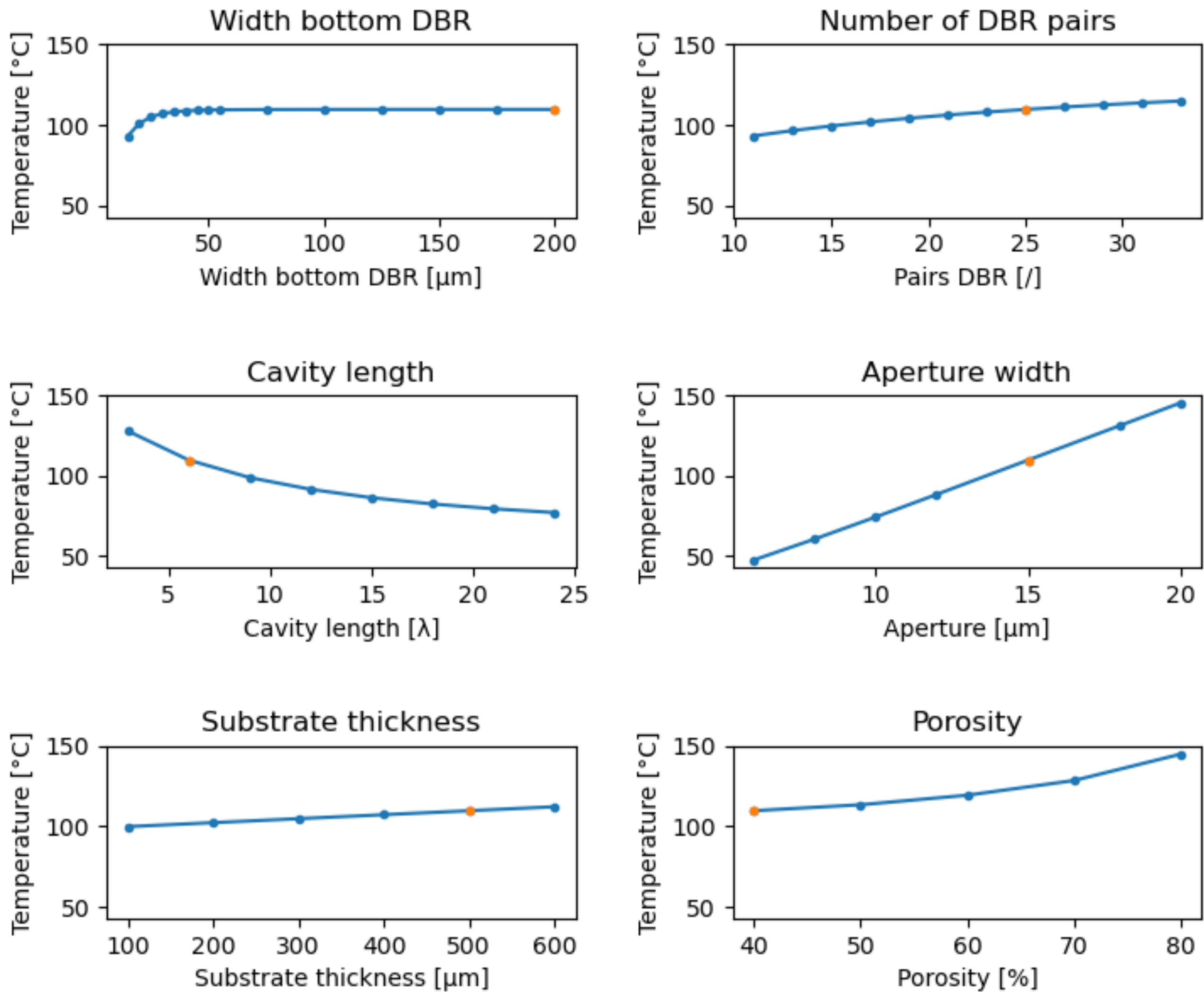

Figure 4.21: Comparison between all the parameters where the orange dot is the reference simulation: Width of bottom DBR = 200 μm, Pairs = 25 , Cavity length = 6λ, Aperture = 15 μm, Substrate thickness = 500 μm and porosity = 40%.

compromise between the thermal and fabrication aspect.

The porosity of the bottom DBR layer is not as easy to analyse as the previous parameters. As explained in subsection 4.1.4, the influence of the porosity is not as important when the diameter of the bottom DBR is confined. A low porosity will allow to reach a lower temperature but a higher porosity allows the mirror to be

more stable, as shown in Figure 4.9. A trade-off can thus be reached by choosing a value of 50% for the confined DBR and 40% for the full DBR. This allows for the confined DBR to have a more stable mirror when working at still acceptable temperatures, since the impact of the porosity is not that important for a confined DBR. This is not the case for a non-confined DBR, this is why a porosity of 40% is chosen to lower the temperature.

By increasing the porosity to 50% for the small DBR, the number of bottom DBR pairs is also lowered to 19 pairs. This will allow to decrease the temperature in the active layer.

The thickness of the substrate is the parameter with the lowest impact, but it has still the ability to reduce the temperature by 10 °C if the thickness of the substrate, which was initially of 500 [μm] is lowered to 100 [μm].

The final optimized structure has thus the following parameters for both confined and full DBR:

1. Bottom DBR width = 15[μm]
2. Number of bottom DBR pairs = 19
3. Porosity = 50%
4. Aperture = 6 [μm]
5. Cavity length = 9 λ
6. Substrate thickness = 100 [μm]

1. Bottom DBR width = 200 [μm]
2. Number of bottom DBR pairs = 25
3. Porosity = 40%
4. Aperture = 6 [μm]
5. Cavity length = 9 λ
6. Substrate thickness = 100 [μm]

The maximum temperature reached in the confined device is 40.08 °C and the large DBR device has a temperature of 41.77 °C. The difference between both values is not very high since the width of the confined DBR is not that small compared to the aperture, but the minimum width is limited by the risk of misalignment.
Final thermal resistance is estimated at 1420 $\frac{°C}{W}$ and 1540 $\frac{°C}{W}$ respectively.
Those values are still higher than what has been reported by others, all values were computed for flipped devices:

- Sony: 2940 $\frac{°C}{W}$ for 8 μm aperture [85] (Value simulated in [8])
- Nichia: 4169 $\frac{°C}{W}$ for 8 μm aperture and 7 λ [32] (Value simulated in [8])

- UCSB: 1400 $\frac{°C}{W}$ for 6 μm aperture and 23 λ [10] (operation temperature of 163 °C)
- Meijo: 710 $\frac{°C}{W}$ for 8 μm aperture and 10λ [64] (maximum lasing temperature of 110 °C)
- NCTU: 708 $\frac{°C}{W}$ for 10 μm aperture and 2.5 λ under a quasicontinuous wave driving condition. [60] (maximum temperature 76.85 °C)

This difference can be explained by the fact that the temperature was decreased to 40 °C by mainly decreasing the aperture. This induces an increase in the thermal resistance as explained in subsection 4.1.5. If the maximum allowed temperature is increased to 51.73 °C for the full DBR, a thermal resistance of 1270 °C/W is reached, by choosing an aperture of 8 μm. For the confined DBR, the maximum temperature for a 8 μm aperture is 50.35 °C and the thermal conductivity is 1213 °C/W.
This is very promising for the future of nanoporous GaN VCSELs to achieve CW operation.

A final computation has been done to simulate the behaviour of the device above the threshold current. This has been done by computing the power density at different current densities, depending on the reported IV curve in [47], shown in Figure 4.22a. The corresponding power density is shown in Figure 4.22b.

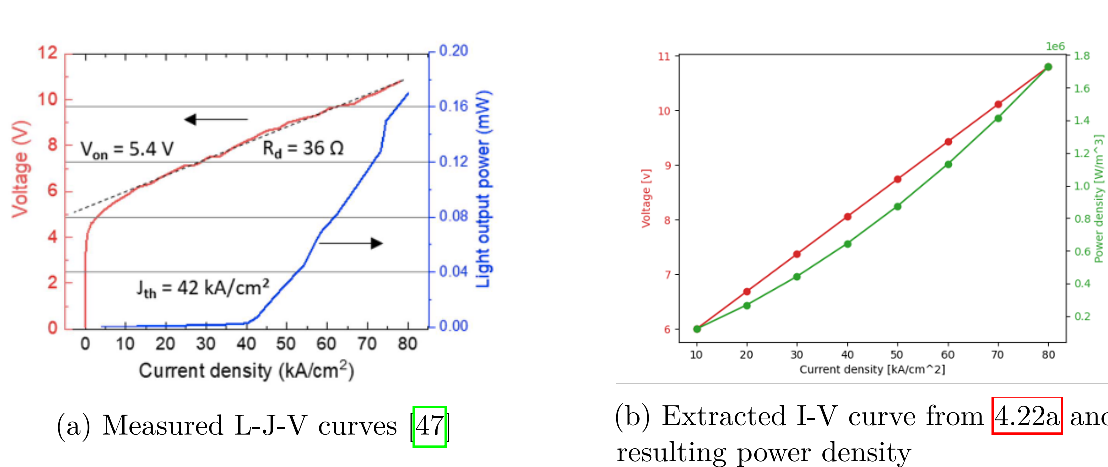

(a) Measured L-J-V curves [47]

(b) Extracted I-V curve from 4.22a and resulting power density

Figure 4.22: Computation of the power density

From the values in Figure 4.22, the temperature reached in the device were simulated and are shown in Figure 4.23

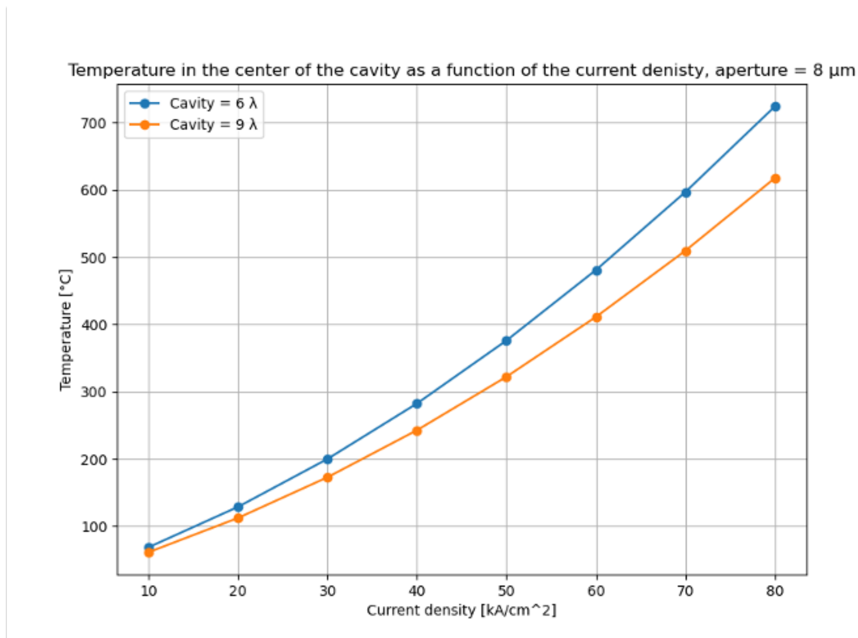

Figure 4.23: Evolution of the temperature in the active region for different current densities

It is clear from the evolution of the curve in Figure 4.23 that the reached temperatures at higher input powers are too high. An additional way to improve the thermal management, other than changing the parameters, is to add a metal pathway in the cavity. Similar solutions have been proposed, as explained in subsection 2.3.3.

4.2.2 Flip-chip

An interesting question to ask is: Can a flip-chip configuration improve the thermal management?

To answer this question, a flip-chip device was simulated with COMSOL, and the device configuration followed the same structure as UCSB, where the device is flipped and a metal pathway around the p-DBR is allowing the heat to flow to the substrate.

The device shown in Figure 4.24 is upside down: the substrate is the top layer in the figure. The heat is mainly flowing through the metal ring around the bottom DBR (p-DBR). By increasing the width of this ring, the temperature inside the cavity is reduced. The temperature in the active region is:

- 237.5 °C for a 0.5 μm wide metal ring.

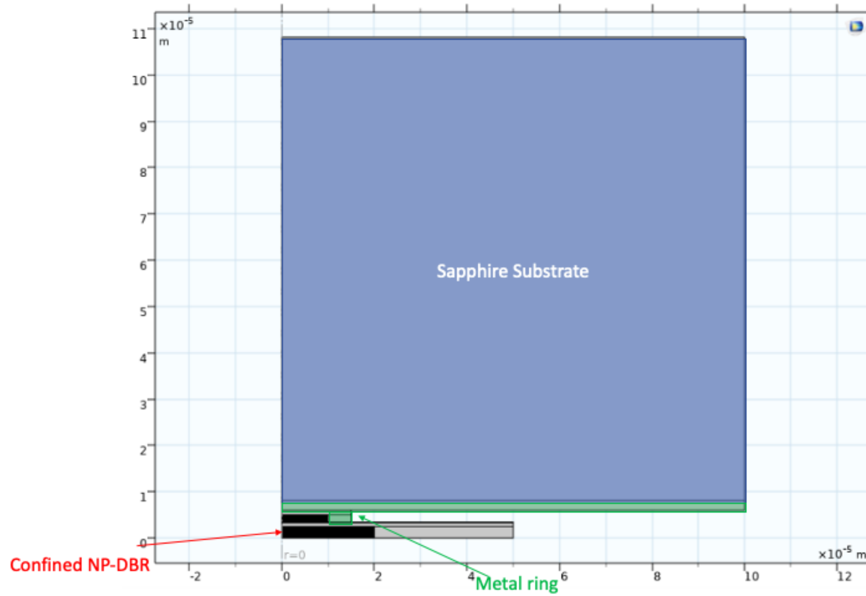

Figure 4.24: Structure of the flipped device.

- 205.5 °C for a 1 μm wide metal ring.
- 111.5 °C for a 5 μm wide metal ring.

The predicted thermal impedance of this device are: 2175, 1855 and 915 °C /W respectively. Even though this computed value seems very promising for the larger ring, it was reported by Forman [50] that their simulated value was lower than the experimental impedance, computed by the redshift of the spontaneous emission. One of the main reason of this difference can be that many simplifications were used for the thermal model of the flipped device. The thermal conductivity of indium was assumed for the Au-In alloys, however Au-In intermetallic layers have a lower thermal conductivity.

The same model as UCSB was used since the NP VCSEL has never been flipped before. The same simplifications were thus used and a higher thermal impedance is thus expected.

A way to improve easily the performance of this flipped device is to change the sapphire substrate (27 W/mK) with a less thermally resistive material like GaN or even copper. Forman [50], reported a simulated improvement of the thermal impedance of 960 °C/W for a 23 λ VCSEL with a silicon carbide substrate.

Chapter 5

Influence of the temperature on optical performances

Contents

5.1 Wavelength shift analysis 76
5.1.1 Transfer Matrix Method (TMM) 76
5.1.2 Matlab program 77
5.1.3 Results 79
5.2 Impact on optical transduction 80

Overview

This chapter analyses the impact of the temperature on important figures of merit of the VCSELs. First a transfer matrix method is explained to compute the wavelength shift. Next the results are compared with values found in the literature. Another important figure of merit is the optical transduction. A review of the impact of the temperature on this value is also done.

5.1 Wavelength shift analysis

An important figure of merit for VCSELs is the induced resonance wavelength shift by the temperature increase. This will be analysed in this section by a one-dimensional transfer matrix method implemented in Matlab. A first simulation is done at room temperature to analyse the resonance wavelength for a constant temperature profile in the whole resonator. Next a varying temperature profile along the optical axis is simulated. The temperature profile is extracted from the previous COMSOL simulations and an average temperature is fixed in each layer of the VCSEL. The thermo-optic coefficient of each layer is then updated respectively to its layer temperature and this new refractive index will then be updated in the Matlab code to analyse the resonance wavelength and thus compute the shift-rate.

As explained in subsection 2.3.2, the thermal wavelength shift is governed by the change in average refractive index in the cavity since the lasing wavelength is more ruled by the resonance wavelength than by the peak gain wavelength.
Computing the wavelength shift with the transfer matrix method based on the change in refractive index is thus a good solution to mitigate the lack of experimental data.

5.1.1 Transfer Matrix Method (TMM)

The reflectivity spectrum and the electric field distribution of a resonator are very important to design efficient VCSELs. Those values can be computed by solving the Helmholtz equation:

$$\frac{\mathrm{d}^2 E(z)}{\mathrm{d}z^2} + \epsilon_r(z)\frac{\omega^2}{c^2}E(z) = 0 \tag{5.1}$$

where E(z) is the phasor of the transverse electric field component. Solving this equation can be done with the transfer matrix method. It allows to analyse the propagation in multilayered structures by computing the interaction of transmitted and reflected waves at each interface of the structure. [87, 22, 25]

In Equation 5.1, the coordinate derivative is only along one direction since the permittivity is only changing along the z-axis. It is thus considered that the light propagates perpendicularly to the layer-to-layer interface in this computation.[87]

The general solution of the Helmholtz equation for j-th layer takes the following form:

$$E_j(z) = A_j e^{jn_j k z_j} + B_j e^{-jn_j k z_j} \tag{5.2}$$

where $k = \frac{2\pi}{\lambda}$, with λ the wavelength, n_j the refractive index of the j-th layer and z_j the thickness of the j-th layer.
Boundary conditions needs to be fixed to solve the Helmholtz equation:

- The amplitude of the forward wave of the incoming light can be chosen: $A_0 = 1$
- After the last interface of the structure there are no more interface, the reflection is thus absent: $B_{N+1} = 0$
- The last two conditions ensure the continuity of the tangential component of the electric field at the interfaces:

$$E_j(x) = E_{j+1}(x) \tag{5.3}$$

$$\frac{\partial}{\partial x} E_j(x) = \frac{\partial}{\partial x} E_{j+1}(x) \tag{5.4}$$

By substituting the general formula (Equation 5.2) into the boundary conditions (Equation 5.3), the resulting becomes:

$$A_j e^{jn_j k z_j} + B_j e^{-jn_j k z_j} = A_{j+1} e^{jn_{j+1} k z_{j+1}} + B_{j+1} e^{-jn_{j+1} k z_{j+1}} \tag{5.5}$$

$$jn_j k A_j e^{jn_j k z_j} - jn_j k B_j e^{-jn_j k z_j} = jn_{n+1} k A_{j+1} e^{jn_{j+1} k z_{j+1}} - jn_{n+1} k B_{j+1} e^{-jn_{j+1} k z_{j+1}} \tag{5.6}$$

The above explained set of equations are now implemented in a Matlab code to solve the resonance in VCSELs cavities.

5.1.2 Matlab program

The Matlab program used to solve the field distribution inside the VCSEL and to compute the reflection and transmission of a multilayer structure using the TMM, is based on the code of Laurent Nevou [88].
The input of the program is a .m file that holds the structure of the VCSEL. Each layer of the VCSEL is defined by four parameters:

1. Thickness
2. Refractive index
3. Thermo-optic coefficient
4. Temperature

The thickness and refractive index n of each layer were already listed before Table 3.3.

The thermo-optic coefficient is the change in refractive index with response to temperature: $\frac{dn}{dT}$. Since at low temperature the second-order behaviour can be neglected, the thermo-optic coefficient will be supposed to be linear. The final input will allow to compute the new refractive index with the following formula:

$$n_{updated} = n_0 + \frac{\mathrm{d}n}{\mathrm{d}T} \times \Delta T \tag{5.7}$$

where n_0 is the refractive index at reference temperature and ΔT is the difference between the input temperature and the reference temperature.
The thermo-optic coefficient of each material is computed by interpolating data extracted from literature around 434 nm:

- The refractive index of SiO_2 = 0.25×10^{-5} [89][90]
- The refractive index of GaN = 1.6×10^{-4} [91]
- The refractive index of ITO = 2.23×10^{-4} [92]
- The refractive index of HfO_2 = $2.4\ \times10^{-4}$ [93]
- The refractive index of $Al_{0.2}Ga_{0.8}N$ = 2×10^{-4} [25]

Once the input values have been introduced, the TMM is solved in the following way:

$$[M] \times [AB] = [D] \tag{5.8}$$

where

- M contains 2N+2 equation from the N layers and N+1 interfaces
- The vector AB = $[A_0;B_0;A_1;B_1\ ...\ A_N;B_N;A_{N+1};B_{N+1}]$
- A_0 is the amplitude of the incoming light
- B_{N+1} is forced to zero as there is no reflection

$$\overbrace{\begin{bmatrix} \ddots & & & & & \\ & \ddots & & & & \\ & & \ddots & & & \\ & & M & & & \\ & & & \ddots & & \\ & & & & \ddots & \\ & & & & & \ddots \end{bmatrix}}^{2N+2 \text{ Unknowns}} \times \begin{bmatrix} \cancel{A_0} \\ B_0 \\ A_1 \\ B_1 \\ \cdots \\ A_j \\ B_j \\ \cdots \\ A_{N+1} \\ \cancel{B_{N+1}} \end{bmatrix} = \begin{bmatrix} -A_0 \\ -A_0 jnkz \\ 0 \\ 0 \\ \cdots \\ 0 \\ 0 \\ \cdots \\ 0 \\ 0 \end{bmatrix}$$

The z axis is discretized in infinitesimal elements each one of length 0.1×10^{-9}m. The reflection is then given by $|B|^2$ and the transmission is obtained with $|A|^2$.

By simulating cavities at multiple wavelengths, the reflectivity spectrum can be calculated with the TMM. The resonance wavelength can then be extracted from the reflection spectrum since this wavelength exhibits high transmittivity. A dip or drop in the reflectivity is observed in the DBR stopband. [94]

5.1.3 Results

A small dip is visible in the reflectivity spectrum at 434 nm. However, this is not as explicit as for other reports (e.g. [94, 22, 95]) This is due to the fact that the Matlab program was computed for integer wavelengths. Once the code was iterated with decimal values, the dips were more explicit, as the resonance of the cavity is 434.1 nm and not 434 nm exactly..

The simulation is first performed for a constant temperature of 20 °C. It is then repeated and all the refractive index are updated depending on the average temperature in the respective layer. This temperature profile has been extracted from Figure 3.5.

The resulting wavelength shift is:

$$\frac{\mathrm{d}\lambda}{\mathrm{d}T} = \frac{437 - 434.1}{110} = 0.026[nm/K] \tag{5.9}$$

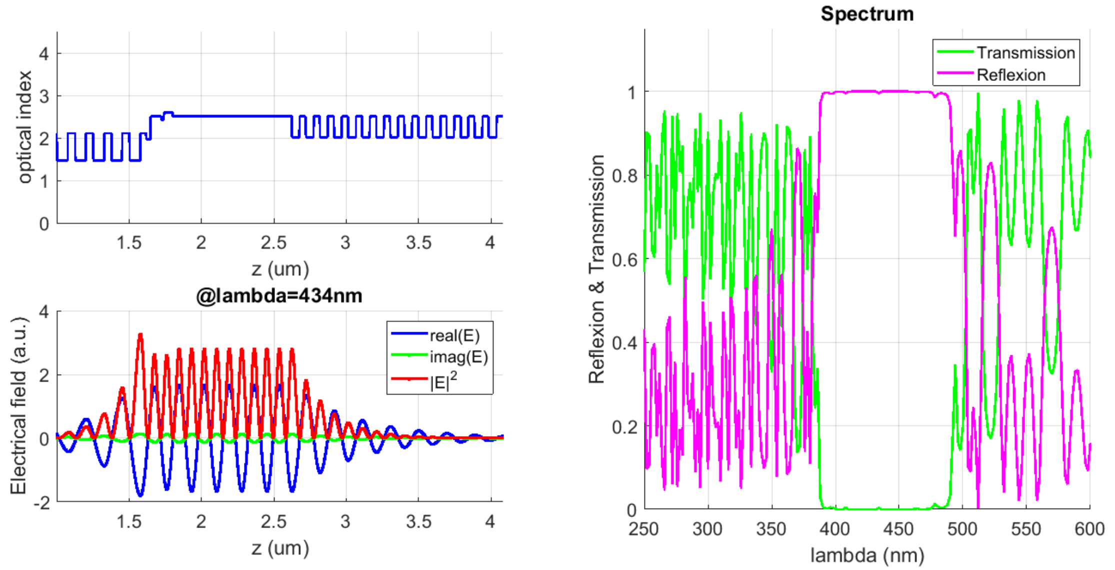

Figure 5.1: Refractive index profile using in the computer simulation along with the generated optical field distribution and the calculated reflectivity spectra of the processed VCSEL wafer.

This is in good agreement with experimental measured values: from 0.012 nm/K [60] to 0.0185 nm/K [9]. However, the computed value is a bit higher than the highest measured shift. This can be explained by the fact that an average of the temperature was done in each layer and that the thermo-optic coefficient were an interpolation of data found in the literature. It is although showing that the mathematical approach is correct.

5.2 Impact on optical transduction

A strong increase in threshold current was observed with increasing temperature. This is directly related to the properties of the multiple quantum wells. The main contribution of the increasing in threshold current was found to be Auger recombination and vertical carrier leakage over the barriers. [15, 56]

As explained, the differential quantum efficiency can be computed by measuring the slope of the P-I curve. This is shown in Figure 5.2 where the VCSEL slope output and differential quantum efficiency as a function of temperature are plotted. The higher threshold current predicts that more heat will be generated with time and decreases both the slope and differential quantum efficiency. [27, 56]

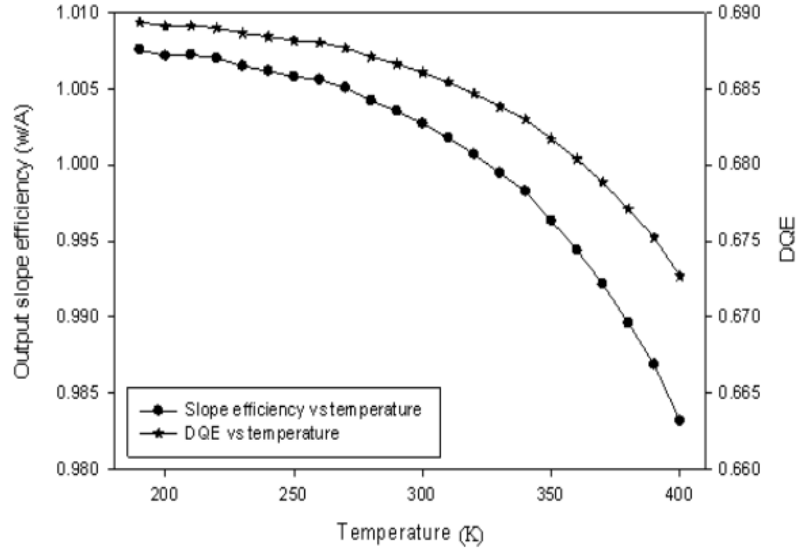

Figure 5.2: VCSEL slope output and differential quantum efficiency as a function of temperature [56]

The temperature dependence of the differential quantum efficiency can be expressed as [62]:

$$\eta_d(T) = \eta_d(300K)e^{\frac{-(T-300)}{T_\eta}} \tag{5.10}$$

with a constant characteristic temperature T_η.

The impact of the temperature can thus be summarized by a shift of the resonant wavelength and also a thermal leakage of the carriers in the active region, leading to an increase of the threshold current density and reduction of the quantum efficiency, contributing to the thermal roll-over. [58] It is thus mandatory to decrease the temperature in the device to avoid all those effects.

Chapter 6

Discussion

It is difficult to discuss about simulation results when no experimental values are available to validate the simulation. This is why all the simulations have been compared with values found in the literature.

As was explained in chapter 2; the common way to improve the thermal management of VCSELs is to increase the cavity length. It has been demonstrated in chapter 3 that is was an efficient way to decrease the temperature.

The aperture although, is the parameter that impacts the most the temperature. But it is related to the injected power and to the geometry. This makes the analysis of this parameter more complicated.
The heat flux analysis showed that the thermal dissipation happens spherically close to the active region and then propagates linearly in the cavity.
Increasing the aperture will thus improve the thermal dissipation of the heat flux which lowers the thermal resistance, but it will also increase the injected power in the device, leading to higher temperatures.

The most interesting parameter to analyse is the porosity since it allows more flexibility than other epitaxial DBRs (e.g. AlInN [64]). It is easy to understand that a higher porosity will decrease the thermal conductivity of the DBR and will thus increase the temperature in the device. However the stability of NP mirrors increases with the porosity, since the refractive index contrast will be higher. A trade-off is thus necessary:
In the case of a confined DBR, the heat flux can get around the DBR. The porosity of the mirror impacts less the temperature in the device than in the case of a full DBR. The porosity of confined DBRs can thus be increased to improve the stability of the mirrors. This cannot be done for DBRs that are larger than 50 μm since the heat flux is mainly passing through the mirror. If the porosity is increased, the

thermal impedance would be increased too.

The impact of the main parameters have thus been discussed and analysed more in details than what have been done in the literature.

The thermal impedance of the optimized VCSEL is expected to be higher in reality. This has been the case for other research groups (e.g. [10]) This can be explained by the hypotheses that have been done: the thermal conductivity did not depend on the doping neither the temperature, while in reality it will have an impact. Next the heat sources were all lumped in the active device.

As has been explained, a flipped VCSEL design is not a good solution to improve the thermal management:

- First because the fabrication of flipped devices is very complicated. As explained in Formans thesis [50]: the Au-In SLID bonding was a key design improvement.
- Next the thermal impedance with a thick Au ring has the same order of magnitude as the improved NP GaN VCSEL.

It is thus a better option to continue to improve the NP GaN-Based VCSEL thermal management.

In chapter 5, the impact on the optical performances was analysed. The thermal wavelength shift has been estimated around 0.026 nm/K, which corresponds with the experimental measured values in the literature.

This wavelength shift can be compensated during the VCSEL design. By designing the VCSEL to have a shorter peak gain wavelength than the Fabry-Perot resonance wavelength, at higher temperatures, the redshifted peak gain provides better mode alignment, reducing the threshold current density. [22]

To summarize all this thesis, a thermal model on COMSOL has been created to analyse the thermal management of nanoporous VCSELs that are very promising. By optimizing the main parameters of the device, the temperature in the active region decreased and the thermal resistance has the same order of magnitude as values that are found in the literature. To allow the device to work at higher current densities, a metal pathway can be added to reduce the thermal impedance even more.

The model that has been created can be used in the future to analyse the thermal performances of other VCSELs.

Chapter 7

Conclusion

Master thesis conclusions

In this master thesis, the main subject has been the improvement of the thermal management in the porous VCSELs. This has been done through SEM simulation on COMSOL.

The impact of each parameter has been analysed and compared to improve the heat dissipation in the device. The main parameters are the aperture and the cavity length. Next a trade-off needs to be made between the porosity and the width of the bottom DBR.

The final optimization results give a thermal impedance of 1420 °C/W. This value is close to other VCSEL that could achieve CW: [64, 60, 50]. This is a great news for the blue GaN-based VCSELs since the fabrication of NP VCSELs is easier to implement than dielectric DBRs and the ECE process that is used to generate the porous layers is a faster process than the typical growth rate of AlInN [28].

Perspectives

The next batch of NP GaN VCSEL are designed with a 8 μm aperture, a cavity length of 6 λ and the DBR is not-confined. By decreasing the aperture, the temperature in the device will be greatly improved. It will be the occasion to verify if the VCSEL is able to achieve CW operation.

If CW is achievable it will be a great improvement in the history of blue GaN-based VCSELs since the fabrication of porous VCSELs is easier and allows vertical injection while dielectrics require lateral current injection through intra-cavity spreading

layers.

If CW is still not reached, a solution would be to increase the cavity length to 9 λ. Another solution would be to add a metal pathway in the cavity to improve the heat dissipation. This would however be more difficult to implement than just increasing the thickness of the n-GaN layer in the cavity.

A future project is to use the COMSOL model to simulate the heat dissipation of InP-based VCSELs that lase at IR wavelengths.

Bibliography

[1] Hsin-chieh Yu et al. “Progress and prospects of GaN-based VCSEL from near UV to green emission”. In: *Progress in Quantum Electronics* 57 (Jan. 2018), pp. 1–19. DOI: 10.1016/j.pquantelec.2018.02.001.

[2] Å. Haglund et al. “Progress and challenges in electrically pumped GaN-based VCSELs”. In: *SPIE Proceedings*. Ed. by Krassimir Panajotov et al. SPIE, Apr. 2016. DOI: 10.1117/12.2229428.

[3] Tatsushi Hamaguchi, Masayuki Tanaka, and Hiroshi Nakajima. “A review on the latest progress of visible GaN-based VCSELs with lateral confinement by curved dielectric DBR reflector and boron ion implantation”. In: *Japanese Journal of Applied Physics* 58.SC (May 2019), SC0806. DOI: 10.7567/1347-4065/ab0f21.

[4] Faten Adel Ismael Chaqmaqchee and James A. Lott. “Impact of oxide aperture diameter on optical output power, spectral emission, and bandwidth for 980 nm VCSELs”. In: *OSA Continuum* 3.9 (Sept. 2020), p. 2602. DOI: 10.1364/osac.397687.

[5] Jim Tatum. “VCSEL proliferation”. In: *SPIE Proceedings*. Ed. by Kent D. Choquette and James K. Guenter. SPIE, Feb. 2007. DOI: 10.1117/12.715082.

[6] LJ Walsh. “The current status of laser applications in dentistry”. In: *Australian Dental Journal* 48.3 (Sept. 2003), pp. 146–155. DOI: 10.1111/j.1834-7819.2003.tb00025.x.

[7] Masoud Panjehpour et al. “Laser-induced fluorescence spectroscopy for in vivo diagnosis of non-melanoma skin cancers”. In: *Lasers in Surgery and Medicine* 31.5 (Nov. 2002), pp. 367–373. DOI: 10.1002/lsm.10125.

[8] Saadat Mishkat-Ul-Masabih et al. “Techniques to reduce thermal resistance in flip-chip GaN-based VCSELs”. In: *physica status solidi (a)* 214.8 (June 2017), p. 1600819. DOI: 10.1002/pssa.201600819.

[9] Yang Mei et al. “A comparative study of thermal characteristics of GaN-based VCSELs with three different typical structures”. In: *Semiconductor Science and Technology* 33.1 (Dec. 2017), p. 015016. DOI: 10.1088/1361-6641/aa90aa.

[10] Charles A. Forman et al. “Continuous-wave operation of m-plane GaN-based vertical-cavity surface-emitting lasers with a tunnel junction intracavity contact”. In: *Applied Physics Letters* 112.11 (Mar. 2018), p. 111106. DOI: 10.1063/1.5007746.

[11] Filip Hjort. “Ultraviolet vertical cavity surface emitting lasers and vertical microcavities for blue lasers”. English. OCLC: 1257840643. PhD thesis. 2021.

[12] Jianwei Ben et al. “2D III-Nitride Materials: Properties, Growth, and Applications”. In: *Advanced Materials* 33.27 (May 2021), p. 2006761. DOI: 10.1002/adma.202006761.

[13] D S Arteev et al. “Investigation of Statistical Broadening in InGaN Alloys”. In: *Journal of Physics: Conference Series* 1135 (Dec. 2018), p. 012050. DOI: 10.1088/1742-6596/1135/1/012050.

[14] Ananta R. Acharya. “Group III – Nitride Semiconductors: Preeminent Materials for Modern Electronic and Optoelectronic Applications”. In: *Himalayan Physics* 5 (June 2015), pp. 22–26. DOI: 10.3126/hj.v5i0.12818.

[15] Joachim Piprek, ed. *Nitride Semiconductor Devices: Principles and Simulation*. Wiley, Jan. 2007. DOI: 10.1002/9783527610723.

[16] Donald Neamen. *Semiconductor Physics and Devices: Basic Principles*. MC-GRAW HILL BOOK CO, Jan. 2011. 784 pp. ISBN: 0073529583. URL: https://www.ebook.de/de/product/13620453/donald_neamen_semiconductor_physics_and_devices_basic_principles.html.

[17] Sadao Adachi. “Lattice thermal conductivity of group-IV and III–V semiconductor alloys”. In: *Journal of Applied Physics* 102.6 (Sept. 2007), p. 063502. DOI: 10.1063/1.2779259.

[18] A Einstein. “The Quantum Theory of Radiation”. In: 1917.

[19] Gerhard Fasol, Shuji Nakamura, and Stephen Pearton. *The Blue Laser Diode*. Springer Berlin Heidelberg, Dec. 2010. 388 pp. ISBN: 3642085792. URL: https://www.ebook.de/de/product/13924498/gerhard_fasol_shuji_nakamura_stephen_pearton_the_blue_laser_diode.html.

[20] Inc. Konica Minolta Sensing Americas. *Characterization of VCSEL arrays including polarization analysis*. URL: https://sensing.konicaminolta.us/us/technologies/vcsel-laser-industry/ (visited on 10/05/2022).

[21] Tal Margalith. “Development of Growth and Fabrication Technology for Gallium Nitride-Based Vertical Cavity Surface Emitting Lasers”. PhD thesis. University of California at Santa Barbara, 2002.

[22] Rainer Michalzik. *VCSELs*. Springer Berlin Heidelberg, Oct. 2012. 580 pp. ISBN: 364224985X. URL: https://www.ebook.de/de/product/16558902/vcsels.html.

[23] Marek Osinski. “Vertical-cavity surface-emitting lasers: effects of heating on modal characteristics and threshold current”. In: *Circular-Grating Light-Emitting Sources*. Ed. by S. Iraj Najafi, Mahmoud Fallahi, and Nasser Peyghambarian. SPIE, Apr. 1995. DOI: 10.1117/12.206346.

[24] *Vertical-Cavity Surface-Emitting Laser Devices*. Springer Berlin Heidelberg, Dec. 2010. 404 pp. ISBN: 3642087434. URL: https://www.ebook.de/de/product/13905082/vertical_cavity_surface_emitting_laser_devices.html.

[25] Giulia Cardinali. *Thermal management of ultraviolet LEDs and VCSELs: computer-aided multiphysics optimization - Webthesis*. 2019. URL: https://webthesis.biblio.polito.it/12449/.

[26] Marcus BENGTHS. “Design of nanowire-based vertical-cavity surface-emitting lasers”. MA thesis. Chalmers University of Technology, 2018.

[27] Larry A. Coldren, Scott W. Corzine, and Milan L. Mašanović. *Diode Lasers and Photonic Integrated Circuits*. John Wiley & Sons, Inc., Mar. 2012. DOI: 10.1002/9781118148167.

[28] Cheng Zhang, Rami ElAfandy, and Jung Han. “Distributed Bragg Reflectors for GaN-Based Vertical-Cavity Surface-Emitting Lasers”. In: *Applied Sciences* 9.8 (Apr. 2019), p. 1593. DOI: 10.3390/app9081593.

[29] Tien-Chang Lu et al. “CW lasing of current injection blue GaN-based vertical cavity surface emitting laser”. In: *Applied Physics Letters* 92.14 (Apr. 2008), p. 141102. DOI: 10.1063/1.2908034.

[30] Gatien Cosendey et al. “Blue monolithic AlInN-based vertical cavity surface emitting laser diode on free-standing GaN substrate”. In: *Applied Physics Letters* 101.15 (Oct. 2012), p. 151113. DOI: 10.1063/1.4757873.

[31] Kazuki Ikeyama et al. “Room-temperature continuous-wave operation of GaN-based vertical-cavity surface-emitting lasers with n-type conducting AlInN/GaN distributed Bragg reflectors”. In: *Applied Physics Express* 9.10 (Sept. 2016), p. 102101. DOI: 10.7567/apex.9.102101. URL: https://doi.org/10.7567/apex.9.102101.

[32] Yu Higuchi et al. "Room-Temperature CW Lasing of a GaN-Based Vertical-Cavity Surface-Emitting Laser by Current Injection". In: *Applied Physics Express* 1 (Dec. 2008), p. 121102. DOI: 10.1143/apex.1.121102.

[33] Shouichiro Izumi et al. "Room-temperature continuous-wave operation of GaN-based vertical-cavity surface-emitting lasers fabricated using epitaxial lateral overgrowth". In: *Applied Physics Express* 8.6 (May 2015), p. 062702. DOI: 10.7567/apex.8.062702.

[34] Tatsushi Hamaguchi et al. "Lateral optical confinement of GaN-based VCSEL using an atomically smooth monolithic curved mirror". In: *Scientific Reports* 8.1 (July 2018). DOI: 10.1038/s41598-018-28418-6.

[35] Cheng Zhang et al. "Mesoporous GaN for Photonic Engineering—Highly Reflective GaN Mirrors as an Example". In: *ACS Photonics* 2.7 (June 2015), pp. 980–986. DOI: 10.1021/acsphotonics.5b00216.

[36] Saadat M. Mishkat-Ul-Masabih et al. "Electrically injected nonpolar GaN-based VCSELs with lattice-matched nanoporous distributed Bragg reflector mirrors". In: *Applied Physics Express* 12.3 (Feb. 2019), p. 036504. DOI: 10.7567/1882-0786/ab0576.

[37] Rami T. ElAfandy et al. "Room-temperature operation of c-plane GaN vertical cavity surface emitting laser on conductive nanoporous distributed Bragg reflector". In: *Applied Physics Letters* 117.1 (July 2020), p. 011101. DOI: 10.1063/5.0012281.

[38] Iwan Sumirat, Y. Ando, and S. Shimamura. "Theoretical consideration of the effect of porosity on thermal conductivity of porous materials". In: *Journal of Porous Materials* 13.3-4 (Aug. 2006), pp. 439–443. DOI: 10.1007/s10934-006-8043-0.

[39] Lei Zhang et al. "One-step fabrication of porous GaN crystal membrane and its application in energy storage". In: *Scientific Reports* 7.1 (Mar. 2017). DOI: 10.1038/srep44063.

[40] Josué Mena et al. "Optical and structural characterisation of epitaxial nanoporous GaN grown by CVD". In: *Nanotechnology* 28.37 (Aug. 2017), p. 375701. DOI: 10.1088/1361-6528/aa7e9d.

[41] S. Sharifi Malvajerdi, A. Salar Elahi, and M. Habibi. "A novel technique based on a plasma focus device for nano-porous gallium nitride formation on P-type silicon". In: *Physics of Plasmas* 24.4 (Apr. 2017), p. 043511. DOI: 10.1063/1.4980859.

[42] Siddulu Naidu Talapaneni et al. "Facile Synthesis of Crystalline Nanoporous GaN Templated by Nitrogen Enriched Mesoporous Carbon Nitride for Friedel-Crafts Reaction". In: *ChemistrySelect* 1.19 (Nov. 2016), pp. 6062–6068. DOI: 10.1002/slct.201601545.

[43] P H Griffin and R A Oliver. "Porous nitride semiconductors reviewed". In: *Journal of Physics D: Applied Physics* 53.38 (July 2020), p. 383002. DOI: 10.1088/1361-6463/ab9570.

[44] Cheng Zhang et al. "Toward Quantitative Electrochemical Nanomachining of III-Nitrides". In: *Journal of The Electrochemical Society* 165.10 (2018), E513–E520. DOI: 10.1149/2.1181810jes.

[45] Cheng Zhang et al. "(Invited) New Directions in GaN Photonics Enabled by Electrochemical Processes". In: *ECS Transactions* 72.5 (Apr. 2016), pp. 47–56. DOI: 10.1149/07205.0047ecst.

[46] *Porous Silicon: From Formation to Application: Formation and Properties, Volume One*. Taylor Francis Ltd., Apr. 2016. 439 pp. ISBN: 1482264552. URL: https://www.ebook.de/de/product/25250329/porous_silicon_from_formation_to_application_formation_and_properties_volume_one.html.

[47] Jung Han, Rami Elafandy, and Jin-ho Kang. "(Invited) Development of Blue Vertical Cavity Surface Emitting Lasers (VCSELs) with Nanoporous GaN". In: *ECS Transactions* 102.3 (May 2021), pp. 17–23. DOI: 10.1149/10203.0017ecst.

[48] Rami Elafandy et al. "GaN blue vertical-cavity surface-emitting lasers using conductive nanoporous distributed Bragg reflectors". In: *Light-Emitting Devices, Materials, and Applications XXV*. Ed. by Martin Strassburg, Jong Kyu Kim, and Michael R. Krames. SPIE, Mar. 2021. DOI: 10.1117/12.2577986.

[49] Saadat Mishkat-Ul-Masabih. "Nonpolar GaN-Based VCSELs with Lattice-Matched Nanoporous Distributed Bragg Reflector Mirrors". In: *Electrical and Computer Engineering ETDs* (July 2019). URL: https://digitalrepository.unm.edu/ece_etds/468.

[50] Charles Forman. "Achieving Continuous-Wave Lasing for Violet m-plane GaN-Based Vertical-Cavity Surface-Emitting Lasers". PhD thesis. University of California at Santa Barbara, June 2018.

[51] Dr Rüdiger Paschotta. *Quasi-continuous-wave Operation*. en. URL: https://www.rp-photonics.com/quasi_continuous_wave_operation.html (visited on 05/22/2022).

[52] Alberto Tibaldi et al. “VENUS: A Vertical-Cavity Surface-Emitting Laser Electro-Opto-Thermal NUmerical Simulator”. In: *IEEE Journal of Selected Topics in Quantum Electronics* 25.6 (Nov. 2019), pp. 1–12. DOI: 10.1109/jstqe.2019.2893755.

[53] Alberto Gullino et al. “Reduced Dimensionality Multiphysics Model for Efficient VCSEL Optimization”. In: *Applied Sciences* 11.15 (July 2021), p. 6908. DOI: 10.3390/app11156908.

[54] G. Chen, M. A. Hadley, and J. S. Smith. “Pulsed and continuous-wave thermal characteristics of external-cavity surface-emitting laser diodes”. In: *Journal of Applied Physics* 76.6 (Sept. 1994), pp. 3261–3271. DOI: 10.1063/1.357447.

[55] G.K. Wachutka. “Rigorous thermodynamic treatment of heat generation and conduction in semiconductor device modeling”. In: *IEEE Transactions on Computer-Aided Design of Integrated Circuits and Systems* 9.11 (1990), pp. 1141–1149. DOI: 10.1109/43.62751.

[56] F. Jasim, K. Omar, and Z. Hassan. “Temperature effect on VCSEL output performance”. In: *Optoelectronics and Advanced Materials, Rapid Communications* 3.11 (2009), pp. 1136–1138.

[57] Joachim Piprek. “Failure analysis of GaN-based current-injected vertical-cavity surface-emitting lasers”. In: *SPIE Proceedings*. Ed. by Joachim Piprek. SPIE, Oct. 2005. DOI: 10.1117/12.631229.

[58] P.V. Mena et al. “A simple rate-equation-based thermal VCSEL model”. In: *Journal of Lightwave Technology* 17.5 (May 1999), pp. 865–872. DOI: 10.1109/50.762905.

[59] Masaru Kuramoto et al. “High-Power GaN-Based Vertical-Cavity Surface-Emitting Lasers with AlInN/GaN Distributed Bragg Reflectors”. In: *Applied Sciences* 9.3 (Jan. 2019), p. 416. DOI: 10.3390/app9030416.

[60] Tsu-Chi Chang et al. “High-temperature operation of GaN-based vertical-cavity surface-emitting lasers”. In: *Applied Physics Express* 10.11 (Oct. 2017), p. 112101. DOI: 10.7567/apex.10.112101.

[61] Masaru Kuramoto et al. “Watt-class blue vertical-cavity surface-emitting laser arrays”. In: *Applied Physics Express* 12.9 (Aug. 2019), p. 091004. DOI: 10.7567/1882-0786/ab3aa6.

[62] MAREK OSIŃSKI and WŁODZIMIERZ NAKWASKI. “THERMAL EFFECTS IN VERTICAL-CAVITY SURFACE-EMITTING LASERS”. In: *Selected Topics in Electronics and Systems*. WORLD SCIENTIFIC, July 1995, pp. 139–202. DOI: 10.1142/9789812830913_0006.

[63] Robert P. Sarzała et al. “Influence of Various Bottom DBR Designs on the Thermal Properties of Blue Semiconductor-Metal Subwavelength-Grating VCSELs”. In: *Materials* 12.19 (Oct. 2019), p. 3235. DOI: 10.3390/ma12193235.

[64] Masaru Kuramoto et al. “High-output-power and high-temperature operation of blue GaN-based vertical-cavity surface-emitting laser”. In: *Applied Physics Express* 11.11 (Oct. 2018), p. 112101. DOI: 10.7567/apex.11.112101.

[65] Seung Geun Lee et al. “Continuous-wave operation of nonpolar GaN-based vertical-cavity surface-emitting lasers”. In: *Gallium Nitride Materials and Devices XIII*. Ed. by Jen-Inn Chyi, Hadis Morkoç, and Hiroshi Fujioka. SPIE, Feb. 2018. DOI: 10.1117/12.2314885.

[66] COMSOL Multiphysics. *Heat Transfer Module User’s Guide*. v. 5.4. 2018.

[67] J. Piprek and S.J.B. Yoo. “Thermal comparison of long-wavelength vertical-cavity surface-emitting laser diodes”. In: *Electronics Letters* 30.11 (1994), p. 866. DOI: 10.1049/el:19940589.

[68] Thomas E. Beechem et al. “Size dictated thermal conductivity of GaN”. In: *Journal of Applied Physics* 120.9 (Sept. 2016), p. 095104. DOI: 10.1063/1.4962010.

[69] H. K. Lee, J. S. Yu, and Y. T. Lee. “Thermal analysis and characterization of the effect of substrate thinning on the peformances of GaN-based light emitting diodes”. In: *physica status solidi (a)* 207.6 (Feb. 2010), pp. 1497–1504. DOI: 10.1002/pssa.200925575.

[70] M. Calciati et al. “Towards a comprehensive 3D VCSEL model: electrical simulations with PICS3D”. In: *2015 Fotonica AEIT Italian Conference on Photonics Technologies*. Institution of Engineering and Technology, 2015. DOI: 10.1049/cp.2015.0143.

[71] H.K. Lee et al. “Thermal analysis of asymmetric intracavity-contacted oxide-aperture VCSELs for efficient heat dissipation”. In: *Solid-State Electronics* 53.10 (Oct. 2009), pp. 1086–1091. DOI: 10.1016/j.sse.2009.06.005.

[72] Jinhui Wang, Ioannis Savidis, and Eby G. Friedman. “Thermal analysis of oxide-confined VCSEL arrays”. In: *Microelectronics Journal* 42.5 (May 2011), pp. 820–825. DOI: 10.1016/j.mejo.2010.11.005.

[73] M. Osiński and W. Nakwaski. “Effective thermal conductivity analysis of 1.55 m InGaAsP/InP vertical-cavity top-surface-emitting microlasers”. In: *Electronics Letters* 29.11 (May 1993), pp. 1015–1016. DOI: 10.1049/el:19930677.

[74] E. W. Lemmon and R. T Jacobsen. "Viscosity and Thermal Conductivity Equations for Nitrogen, Oxygen, Argon, and Air". In: *International Journal of Thermophysics* 25.1 (Jan. 2004), pp. 21–69. DOI: 10.1023/b:ijot.0000022327.04529.f3.

[75] *Refractive index database*. URL: https://refractiveindex.info/ (visited on 05/19/2022).

[76] Taofei Zhou et al. "Thermal transport of nanoporous gallium nitride for photonic applications". In: *Journal of Applied Physics* 125.15 (Apr. 2019), p. 155106. DOI: 10.1063/1.5083151.

[77] *Refractive Index of ITO, Indium Tin Oxide, InSnO for Thin Film Thickness Measurement*. URL: https://www.filmetrics.com/refractive-index-database/ITO/Indium-Tin-Oxide-InSnO (visited on 05/19/2022).

[78] J. F. Muth et al. "Absorption Coefficient and Refractive Index of GaN, AlN and AlGaN Alloys". In: *MRS Internet Journal of Nitride Semiconductor Research* 4.S1 (1999), pp. 502–507. DOI: 10.1557/s1092578300002957.

[79] M. Anani et al. "InxGa1-xN refractive index calculations". In: *Microelectronics Journal* 38.2 (Feb. 2007), pp. 262–266. DOI: 10.1016/j.mejo.2006.11.001.

[80] Artur Wiatrowski et al. "Characterization of HfO2 Optical Coatings Deposited by MF Magnetron Sputtering". In: *Coatings* 9.2 (Feb. 2019), p. 106. DOI: 10.3390/coatings9020106.

[81] Rami T. Elafandy et al. "Study and Application of Birefringent Nanoporous GaN in the Polarization Control of Blue Vertical-Cavity Surface-Emitting Lasers". In: *ACS Photonics* 8.4 (Apr. 2021), pp. 1041–1047. DOI: 10.1021/acsphotonics.1c00211.

[82] Jing Zhang et al. "Characterizations of Seebeck coefficients and thermoelectric figures of merit for AlInN alloys with various In-contents". In: *Journal of Applied Physics* 109.5 (Mar. 2011), p. 053706. DOI: 10.1063/1.3553880.

[83] Hua Tong et al. "Thermoelectric properties of lattice-matched AlInN alloy grown by metal organic chemical vapor deposition". In: *Applied Physics Letters* 97.11 (Sept. 2010), p. 112105. DOI: 10.1063/1.3489086.

[84] J Strnad and A Vengar. "Stefans measurement of the thermal conductivity of air". In: *European Journal of Physics* 5.1 (Jan. 1984), pp. 9–12. DOI: 10.1088/0143-0807/5/1/003.

[85] Tatsushi Hamaguchi et al. "Milliwatt-class GaN-based blue vertical-cavity surface-emitting lasers fabricated by epitaxial lateral overgrowth". In: *physica status solidi (a)* 213.5 (Jan. 2016), pp. 1170–1176. DOI: 10.1002/pssa.201532759.

[86] Xin-She Yang. *Genetic Algorithms*. 2021. DOI: 10.1016/b978-0-12-821986-7.00013-5.

[87] Igor V. Guryev Igor A. Sukhoivanov. *Photonic Crystals*. Springer-Verlag GmbH, Sept. 2009. 242 pp. ISBN: 9783642026461. URL: https://www.ebook.de/de/product/25408612/igor_a_sukhoivanov_igor_v_guryev_photonic_crystals.html.

[88] Laurent NEVOU. *Light_WaveTransmission1D*. https://github.com/LaurentNevou/Light_WaveTransmission1D.git. Apr. 2022 [Online].

[89] Junbo Gong et al. "Temperature dependent optical constants for SiOsub2/sub film on Si substrate by ellipsometry". In: *Materials Research Express* 4.8 (Aug. 2017), p. 085005. DOI: 10.1088/2053-1591/aa7d17.

[90] Ali W. Elshaari et al. "Thermo-Optic Characterization of Silicon Nitride Resonators for Cryogenic Photonic Circuits". In: *IEEE Photonics Journal* 8.3 (June 2016), pp. 1–9. DOI: 10.1109/jphot.2016.2561622.

[91] Naoki Watanabe, Tsunenobu Kimoto, and Jun Suda. "Thermo-Optic Coefficients of 4H-SiC, GaN, and AlN for Ultraviolet to Infrared Regions up to 500
{\circ}*C*". In: *Japanese Journal of Applied Physics* 51 (Oct. 2012), p. 112101. DOI: 10.1143/jjap.51.112101.

[92] Abian B. Socorro et al. "Temperature sensor based on a hybrid ITO-silica resonant cavity". In: *Optics Express* 23.3 (Jan. 2015), p. 1930. DOI: 10.1364/oe.23.001930.

[93] G. He et al. "Optical and electrical properties of plasma-oxidation derived HfO 2 gate dielectric films". In: *Applied Surface Science* 253.7 (Jan. 2007), pp. 3413–3418. DOI: 10.1016/j.apsusc.2006.07.055.

[94] Tetsuya Takeuchi et al. "GaN-based vertical-cavity surface-emitting lasers with AlInN/GaN distributed Bragg reflectors". In: *Reports on Progress in Physics* 82.1 (Nov. 2018), p. 012502. DOI: 10.1088/1361-6633/aad3e9.

[95] John T. Leonard. "Vertical-Cavity Surface-Emitting Lasers". PhD thesis. University of California, Santa Barbara, 2016.

UNIVERSITÉ CATHOLIQUE DE LOUVAIN
École polytechnique de Louvain
Rue Archimède, 1 bte L6.11.01, 1348 Louvain-la-Neuve, Belgique | **www.uclouvain.be/epl**